

GA-NIFS: Dissecting The Alchemised: NIRSpec/IFU reveals turbulent gas inflows in a complex system at $z = 10.17$

Robert G. Pascalau, ^{★1,2} Francesco D’Eugenio, ^{1,2} Roberto Maiolino, ^{1,2,3} Qiao Duan, ^{1,2} Yuki Isobe, ^{1,2,4} Santiago Arribas, ⁵ Andrew J. Bunker, ⁶ Stéphane Charlot, ⁷ Michele Perna, ⁵ Bruno Rodríguez Del Pino, ⁵ Hannah Übler, ⁸ Elena Bertola, ⁹ Torsten Böker, ¹⁰ Stefano Carniani, ¹¹ Dan Coe, ^{10,12,13} Giovanni Cresci, ⁹ Mirko Curti, ¹⁴ Tiger Y.Y. Hsiao, ¹⁵ Lucy R. Ivey, ^{1,2} Gareth C. Jones, ^{1,2} Isabella Lamperti, ^{9,16} Eleonora Parlanti, ¹¹ Jan Scholtz, ^{1,2} Sandro Tacchella, ^{1,2} Lorenzo Ulivi, ⁵ Giacomo Venturi, ¹¹ Joris Witstok ^{17,18} and Sandra Zamora ¹¹

Affiliations are listed at the end of the paper.

ABSTRACT

Recent observations revealed that distant galaxies have bursty star formation histories, regulated by stellar or active galactic nuclei (AGN) feedback and gas inflows. According to theoretical models, feedback preferentially removes metal-rich gas, while subsequent starbursts are triggered by mergers and newly-accreted gas that is generally less enriched than the galaxy interstellar medium (ISM). Therefore, gas-phase metallicity holds key insights into the baryonic processes shaping early galaxies. We present the first NIRSpec/IFU study of spatially resolved ISM properties in the MACS0647-JD system ($z = 10.17$). The system consists of two stellar components detected in NIRSpec/IFU and NIRCам photometry. The main component ($\log(M_*/M_\odot) = 7.77 \pm 0.09$; $12 + \log(O/H) = 7.89 \pm 0.11$) is more massive and significantly more metal-rich compared to its companion ($\log(M_*/M_\odot) = 7.42 \pm 0.07$; $12 + \log(O/H) = 7.47 \pm 0.14$), suggesting an older stellar population and a prolonged chemical enrichment history. We find that the H γ line emission centroid is spatially offset by $\sim 0.1''$ (150 pc in the source plane) from the stellar continuum centroid; the latter coincides with the location of the main stellar component. This offset provides possible evidence of a merger-driven starburst in this system. By comparing the spatial distribution of the metallicity, velocity dispersion, and the burstiness of star formation history, we infer the presence of turbulent, metal-poor gas outside the stellar components. This metal-poor, dynamically unstable gas is likely responsible for the increase in the recent star formation in the north-east region of the system.

Key words: galaxies: high redshift – galaxies: evolution – galaxies: abundances – galaxies: ISM – ISM: kinematics and dynamics

1 INTRODUCTION

Theoretical models posit that early galaxies had variable star formation histories (SFHs), characterised by multiple episodes of intense star formation, each followed by spans of lower activity (Ma et al. 2018; Faucher-Giguère 2018; Iyer et al. 2020; Tacchella et al. 2020; Dome et al. 2024; McClymont et al. 2025a). *JWST* observations are confirming this picture, with the discovery of a plethora of galaxies in each of these phases: starbursts (Boyett et al. 2024; Dressler et al. 2024; Langeroodi & Hjorth 2024; Endsley et al. 2025; Looser et al. 2025; Witten et al. 2025) and quenched (Strait et al. 2023; Looser et al. 2024; Baker et al. 2025; Covelo-Paz et al. 2026). One of the key tracers of star formation histories is the gas-phase metallicity, which carries the imprint of a number of mechanisms shaping the evolution of galaxies before the Cosmic Noon (Davé et al. 2011; Lilly et al. 2013; Somerville & Davé 2015; Péroux & Howk 2020). SFHs are regulated by a combination of baryonic processes, including mergers, cosmological gas accretion, and gas outflows due to stellar (Baker et al. 2023; Zamora et al. 2025a) or active galactic nuclei (AGN) feed-

back (Fabian 2012; Weinberger et al. 2017; Bourne & Yang 2023). Such outflows can efficiently remove metal-enriched gas and suppress star formation, leading to quiescent phases (Fabian 2012; Hopkins et al. 2014, 2023). Conversely, mergers and metal-poor inflows of dense gas can rejuvenate galaxies by triggering intense episodes of star formation (Kereš et al. 2005; Dekel et al. 2009; Schaye et al. 2010; Sparre et al. 2017; Sun et al. 2023; Langeroodi & Hjorth 2023; Mason et al. 2023; Yajima et al. 2023).

It was suggested that gas accretion and bursty star formation lead to an increased scatter of the mass–metallicity relation (MZR; Tremonti et al. 2004; Kewley & Ellison 2008; Maiolino et al. 2008; Sánchez et al. 2017), as reported by simulations (De Rossi et al. 2017; Agertz et al. 2020; Garcia et al. 2024) and semi-analytical models (e.g., De Lucia et al. 2020). Furthermore, simulations reveal a link between stellar feedback and spatial distribution of metals: enhanced stellar feedback models lead to efficient mixing of metals in the interstellar medium (ISM), which means that radial metallicity gradients are flatter on average in these cases (Gibson et al. 2013; Mott et al. 2013; Garcia et al. 2025; Sun et al. 2025). However, such metallicity gradients are physically stable only if those systems evolved long enough to reach a nearly steady state. Observational evidence of

* E-mail: rgp34@cam.ac.uk

whether correlations between very recent star formation activity and metallicity exist on spatially resolved scales in the early Universe is scarce (e.g. Marconcini et al. 2024).

Following the launch of James Webb Space Telescope (*JWST*; Gardner et al. 2023; Rigby et al. 2023), it became possible to study rest-frame optical and near-infrared spectra and photometry of distant galaxies less than 1 Gyr after Big-Bang (Bunker et al. 2023; Curtis-Lake et al. 2023; Fujimoto et al. 2023; Kashino et al. 2023; Oesch et al. 2023; Roberts-Borsani et al. 2023; Robertson et al. 2023; Wang et al. 2023b; Bunker et al. 2024; D’Eugenio et al. 2024b; Fujimoto et al. 2024; Hainline et al. 2024; Harikane et al. 2024; D’Eugenio et al. 2025b; Donnan et al. 2025; Marconcini et al. 2025; Napolitano et al. 2025; Price et al. 2025) even up to $z > 14$ (< 300 Myr before the Big Bang; Carniani et al. 2024; Naidu et al. 2025). In order to understand how galaxies evolve across cosmic time, it is necessary to constrain the properties of their interstellar media (ISM).

Owing to its unprecedented near-infrared sensitivity, and its capabilities to provide high spatial resolution (sub-kpc scales) and $R \sim 1000 - 3000$ spectra unaffected by telluric lines and atmospheric effects, *JWST*/NIRSpec (Jakobsen et al. 2022) completely revolutionised our understanding of galaxy formation and evolution before Cosmic Noon. These early galaxies have truly extreme ISM conditions, including hard radiation fields, high ionisation parameter (Cameron et al. 2023; Mascia et al. 2023; Sanders et al. 2023b; Tang et al. 2023; Boyett et al. 2024; Calabrò et al. 2024; Topping et al. 2024, 2025b), high electron number density (Isobe et al. 2023b; Reddy et al. 2023; Li et al. 2025; Topping et al. 2025a) or higher electron temperatures combined with lower metallicities compared to lower- z galaxies of similar M_* and star formation rate (Langeroodi et al. 2023; Trump et al. 2023; Curti et al. 2024; Laseter et al. 2024; Pollock et al. 2025). All these observational results are in agreement with the findings of theoretical hydrodynamical simulations like MEGATRON (Choustikov et al. 2025). Moreover, *JWST* observations substantially increased the number of $2 < z < 10$ auroral line detections (Curti et al. 2023; Nakajima et al. 2023; Laseter et al. 2024; Morishita et al. 2024; Sanders et al. 2024; Scholte et al. 2025; Shapley et al. 2025; Stiavelli et al. 2025) allowing for an accurate calculation of gas-phase metallicities based on the direct- T_e method (Osterbrock 1989; Kewley & Ellison 2008). Capitalising on the capabilities of the integral-field unit (IFU) mode of the NIRSpec instrument (Böker et al. 2022) to reveal spatial and spectral information, a number of recent studies focused on spatially resolved gas-phase metallicity and ISM properties in galaxies at $z = 2 - 8$. One key strength of IFU studies is the ability to provide in-depth analyses of systems with complex morphologies and intricate kinematics (Rodríguez Del Pino et al. 2024; Jones et al. 2024a,b; Übler et al. 2024; Jones et al. 2025c; Marshall et al. 2025a; Parlanti et al. 2025b; Pérez-González et al. 2025; Scholtz et al. 2025b; Zamora et al. 2025b) including the discovery of dual/multiple AGN (Perna et al. 2025; Übler et al. 2025). A robust characterisation of the true nature of such systems is challenging without IFU spectroscopy (D’Eugenio et al. 2025d).

At higher redshifts, galaxies are on average smaller than their low- z counterparts, as demonstrated by observations (e.g., Shibuya et al. 2015; Huertas-Company et al. 2024; Matharu et al. 2024; Danhaive et al. 2025a; Miller et al. 2025; Stephenson et al. 2025; Yang et al. 2025) and recent simulations (e.g., Roper et al. 2022; Costantin et al. 2023; Shen et al. 2024; McClymont et al. 2025b). Resolving the ISM in such compact early galaxies is therefore difficult, except in cases when gravitational lensing enables a high enough magnification to resolve otherwise inaccessible physical scales (Mowla et al. 2022; Claeysens et al. 2023; Vanzella et al. 2023; Hsiao et al. 2024a; Mowla et al. 2024; Fujimoto et al. 2025b). Furthermore, additional

caution needs to be taken when interpreting metallicity gradients and ISM properties in high- z targets, because a substantial fraction of them are either formed of multiple clumps (Le Fèvre et al. 2020; Herrera-Camus et al. 2025) or are captured during a merger event (as expected given the increasing merger rates at higher redshifts; Duan et al. 2025; Puskás et al. 2025b) during which gas and metals are re-distributed across the system.

MACS0647-JD is a star-forming galaxy (SFG) at $z_{\text{spec}} = 10.17$ (Hsiao et al. 2023, 2024a), with a stellar mass of $\log(M_*/M_\odot) = 8.1 \pm 0.3$. Its instantaneous star-formation rate (SFR) $\text{SFR}_{\text{H}\alpha} = 5.0 \pm 0.6 M_\odot \text{ yr}^{-1}$ (Hsiao et al. 2024b) places this galaxy 0.6–0.8 dex above the star-forming main sequence at its redshift (e.g., McClymont et al. 2025a), implying that the galaxy is undergoing a starburst episode. The system is triply lensed by the foreground galaxy cluster MACSJ0647.7+7015 ($z = 0.597$; Ebeling et al. 2007). In this study, we analyse the highest-magnification image, MACS0647-JD1 ($\mu = 8 \pm 1$; Chan et al. 2017). This system consists of two closely separated main components (MACS0647-JD A and B) with a third component C at a larger distance from this pair (Hsiao et al. 2023). It was furthermore determined (based on integrated aperture spectroscopy) that component A of the system has a gas-phase metallicity of $12 + \log(O/H) = 7.79 \pm 0.09$ (Hsiao et al. 2024b) and an ionisation parameter $\log(U) = -1.9 \pm 0.2$, highlighting a metal-poor, but strongly ionised ISM, in line with other high-redshift observations (Bunker et al. 2023; Castellano et al. 2024; Curti et al. 2025). However, no conclusion has been reached about the kinematic properties and the interactions between the two main components of this system, leaving the question open of whether they are different components in a merger or just gas clumps in a rotating disc. In this work, we will present NIRSpec/IFU medium-resolution spectroscopy of this target, and we will argue that the former scenario is more likely.

This paper is organised as follows: in Section 2, we discuss the data reduction pipeline, outlining the pre-processing that we did on raw data before using it in our analysis. Section 3 describes our point-spread-function (PSF) matching algorithm for spaxel spectra and the methods that we used for fitting emission lines in the datacube, both spaxel-by-spaxel, as well as by extracting from custom apertures. Section 4 also illustrates various parts of our analysis and highlights key results. Section 5 discusses the most probable nature of the MACS0647-JD system based on its resolved star formation histories, gas kinematics and ISM properties. Our conclusions are outlined in Section 6. We assume a flat Λ CDM cosmology with $H_0 = 67.4 \text{ km s}^{-1} \text{ Mpc}^{-1}$ and $\Omega_m = 0.315$ (Planck Collaboration et al. 2020), giving a physical scale of $4.2 \text{ kpc arcsec}^{-1}$ at redshift $z = 10.17$ (before applying the lensing correction), corresponding to $1.5 \text{ kpc arcsec}^{-1}$ in the source plane (with our assumed magnification of $\mu \sim 8$). Stellar masses are total stellar mass formed, assuming a Chabrier (2003) initial mass function (IMF), integrated between 0.1 and $120 M_\odot$. All magnitudes are in the AB system: $\text{AB mag} = 31.4 - 2.5 \times \log F_{\text{NIR}} \text{ Jy}$ (Oke & Gunn 1983) and all EWs are in the rest frame, with negative EW corresponding to line emission. All the logarithms in this paper are base-10 logarithms: $\log \equiv \log_{10}$.

2 DATA

2.1 NIRSpec/IFU observations

MACS0647-JD (ICRS coordinates of the MACS0647-JD1 image analysed in this paper: R.A. = $06^{\text{h}}47^{\text{m}}55.746^{\text{s}}$; Dec. = $+70^\circ 14' 35.93''$) was first observed by Hubble Space Telescope using the Wide Field Camera 3 (WFC3; Kimble et al. 2008) and Advanced

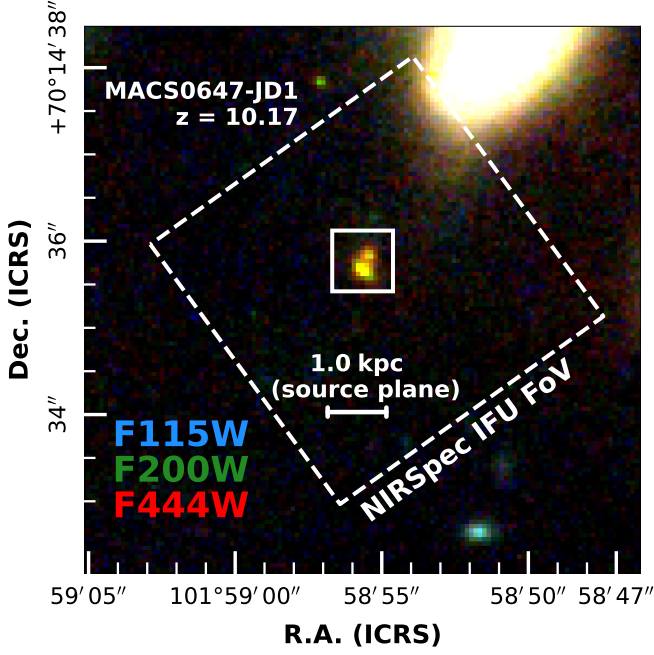


Figure 1. Composite RGB image of MACS0647-JD1 target obtained by superposing F115W, F200W and F444W NIRCcam photometry images. We also overlay the field-of-view of our IFU observations (dashed square), as well as the central $0.7'' \times 0.7''$ aperture (solid square), used for determining the integrated spectrum emission line fluxes and ISM properties. As discussed in Section 3.2, we only fit the emission lines in the spectra of spaxels contained within this aperture.

Camera for Surveys (ACS; Ford et al. 2003); at the time, it was one of the most distant photometric candidates (Coe et al. 2013). Spectroscopic confirmation was obtained with *JWST* ten years later (Hsiao et al. 2024a). Our observations are part of Galaxy Assembly with NIRSpect Integral Field Spectroscopy¹ (GA-NIFS; PIs: S. Arribas and R. Maiolino). This is a NIRSpect/IFU Guaranteed Time Observations programme and our target is included in the *JWST* Cycle 3 Program ID #4528 (PI: K. Isaak). The observations use the medium-resolution G395M/F290LP disperser/filter setup. We used a medium-cycling pattern with 8 dithers, 27 groups per integration and one integration per exposure (with the NRSIRS2 readout mode; Rauscher et al. 2017) giving an on-source time of 4.4 h.

2.2 NIRSpect data reduction and processing

The data reduction uses the *JWST* Science calibration pipeline v1.17.1 with CRDS jwst_1322.pmap. To improve the quality of the datacube, we performed a number of further data processing steps, in addition to the default pipeline. The customised procedures used for cosmic rays snowballs flagging and pink noise (1/f noise) corrections are described in detail in Perna et al. (2023) and Kashino et al. (2023). These were applied to the Stage 1 count-rate products, before the stage 2 and stage 3 calibrations. For the outliers removal, we use the outlier-detection algorithm described in D’Eugenio et al. (2024a, see also Übler et al. 2023) and executed after Stage 2. This algorithm is adapted from the original LACOSMIC (van Dokkum 2001). The background subtraction is the same as described in Pascalau et al. (2025), but here we used H γ and [Ne III] λ 3869 to obtain the source

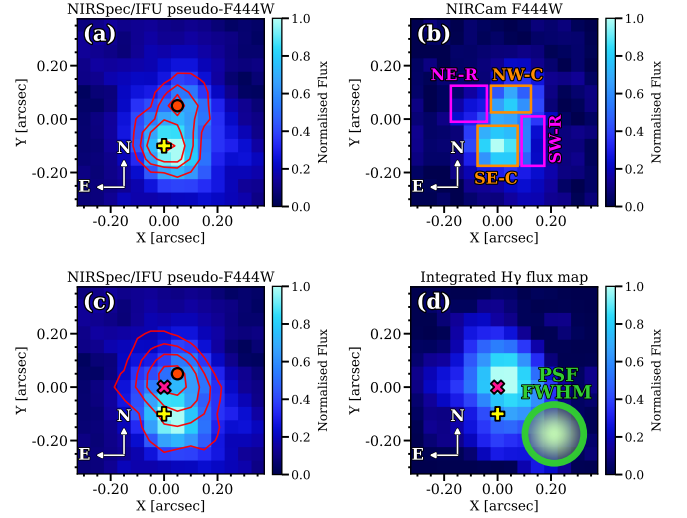


Figure 2. The top panels show the astrometric alignment between the ICRS coordinates of the NIRSpect/IFU synthetic F444W image (Fig. 2a) and the original NIRCcam F444W photometry (Fig. 2b). In Fig. 2a, we overlay contours from the normalised NIRCcam imaging data at 0.3, 0.5, 0.7, and 0.9 times the peak flux (defined by the stellar continuum centroid). We also highlight the brightest spaxels in the two clumps in the system: south-east (yellow ‘+’ cross) and north-west (red circle). The orange rectangles in Fig. 2b approximately mark the apertures corresponding to the SE and NW clumps, while the magenta rectangles indicate the regions outside the main stellar components. In Fig. 2c, we overlay the contours from the normalised H γ integrated flux map (at the same fractional levels as in the top-left panel) on the synthetic F444W image from the datacube. We highlight the centroids of the south-east and north-west clumps (yellow star and red circle), together with the centroid of H γ emission (pink ‘x’ cross). All the panels are shown in arcsecond offsets relative to the H γ emission centroid. The same coordinate convention is adopted for all our subsequent maps in this paper. We also indicate the PSF FWHM (determined as described in Section 3.1) with a circle of diameter equal to the FWHM, shown with a green edge and pale green Gaussian shading to illustrate our assumption of a two-dimensional Gaussian PSF.

mask. The datacube is obtained using the CUBE_BUILD algorithm with a pixel size of $0.05''$ and ‘drizzle’ weighting.

2.3 Imaging and Photometry

We retrieved NIRCcam photometric data from the DAWN *JWST* Archive v7.0 (DJA; Heintz et al. 2025). We used v7.0 MACS0647 mosaics for the filters F115W, F150W, F200W, F277W, F356W and F444W. These imaging data were obtained as part of the *JWST* Cycle 1 Program ID #1433 (PI: D. Coe). Data reduction procedures have been explained in detail by Brammer (2023) and Valentino et al. (2023). We produced $3'' \times 3''$ cutouts (similar to the IFU field-of-view) and applied background subtraction. We first removed the bright sources using a 3σ mask produced with the SIGMACLIP algorithm from ASTROPY (Astropy Collaboration et al. 2022). We then use BACKGROUND2D from PHOTUTILS (Bradley et al. 2024) to divide the masked cutouts into $0.35'' \times 0.35''$ regions. We use MEDIANBACKGROUND as our background estimator. The background values from neighbouring background calculation regions are smoothed using a median filter and interpolated across the full image to produce a full 2-dimensional background image.

¹ <https://ga-nifs.github.io/>

2.4 Astrometry re-alignment of the datacube

The field-of-view of NIRSpec/IFU pointing is $3.1'' \times 3.1''$ which is large enough to contain our target even without an accurate pointing procedure. The no target acquisition mode provides an astrometric precision of $\sim 0.1''$ (Perna et al. 2023; Übler et al. 2023). Because our study focuses on spatially resolved ISM properties, we refine the NIRSpec/IFU astrometry by matching the synthetic F444W image obtained from the datacube to the NIRCам F444W imaging data. This filter was chosen because its wavelength range covers the brightest span of the rest-frame optical continuum in young stellar populations, as well as key rest-frame optical emission lines in our spectra that we want to map and study in detail. We find an offset of $0.19''$ between NIRCам astrometry and our IFU data, comparable to other studies (Arribas et al. 2024; Lamperti et al. 2024; Übler et al. 2024; Fujimoto et al. 2025a,b; Parlanti et al. 2025b). In Fig. 2, we mark the brightest spaxel in the synthetic-F444W image with the yellow ‘+’ cross mark. We can regard this spaxel as the centroid of the stellar continuum light. However, the peak line emission centroid for both H γ and [Ne III] $\lambda 3869$ (marked with a pink ‘x’ cross) is offset by $0.1''$ from the stellar continuum centroid. We will further discuss this spatial offset, together with the different morphology of continuum and line emission in Section 5.1.

2.5 Wavelength range extension and H β recovery

The nominal wavelength range of NIRSpec G395M reaches $\lambda = 5.27 \mu\text{m}$. However, wavelengths $\lambda \lesssim 5.5 \mu\text{m}$ are still recorded on the detector, and can thus be recovered, which is particularly useful for the brightest emission lines at high redshifts. This possibility of extending the recovered wavelength coverage beyond the nominal range has been demonstrated by several recent studies (D’Eugenio et al. 2025a; Torralba et al. 2025 using high-resolution data; Parlanti et al. 2025a; Valentino et al. 2025 using medium-resolution data). In this work, we aim to measure H β , with a method similar to D’Eugenio et al. (2025a), but focusing on the red end of the G395M grating.

At $z \sim 10.17$, H β emission lies at $\lambda_{\text{obs}} \approx 5.43 \mu\text{m}$, outside the nominal wavelength range covered by G395M / F290LP disperser/filter setup. The line is well detected because the F290LP filter does not suppress longer wavelengths and the transmission of the grating does not drop sharply beyond $\lambda_{\text{obs}} > 5.27 \mu\text{m}$ (D’Eugenio et al. 2025a). On the other hand, the [O III] $\lambda\lambda 4959, 5007$ doublet lines would fall at observed wavelengths of $\approx 5.54 \mu\text{m}$ and $\approx 5.59 \mu\text{m}$ respectively. At these wavelengths, the detector efficiency decreases, suppressing the [O III] $\lambda\lambda 4959, 5007$ emission, which is therefore not detected. We extract the spectra by extrapolating the flat-field curves and the wavelength calibration solution beyond the nominal range. There are only 89 spectral pixels (in the case of our medium-resolution grating) between H β observed wavelength and the red end of the nominal spectral range. As a result of the well characterised behaviour of the grating, the error on the wavelength solution is small.

To derive the flux calibration of our extended data, we rely on extrapolating the background level. We perform an initial data reduction where we extend the existing calibration files for the flat-field correction and flux calibration. We use initially a linear extrapolation of the existing calibrations to the range $5.27\text{--}5.55 \mu\text{m}$. The calibrations consist of an illumination flat, a detector flat, and a spectrograph flat. After this initial step, the resulting datacube displays a sharp drop at $\lambda \gtrsim 5.35 \mu\text{m}$. This is shown in Fig. 3a, where the grey spectrum was extracted in an empty circular aperture of the initial datacube. Since the signal in this region is expected to increase smoothly with wavelength, we use data in the well-calibrated spectral

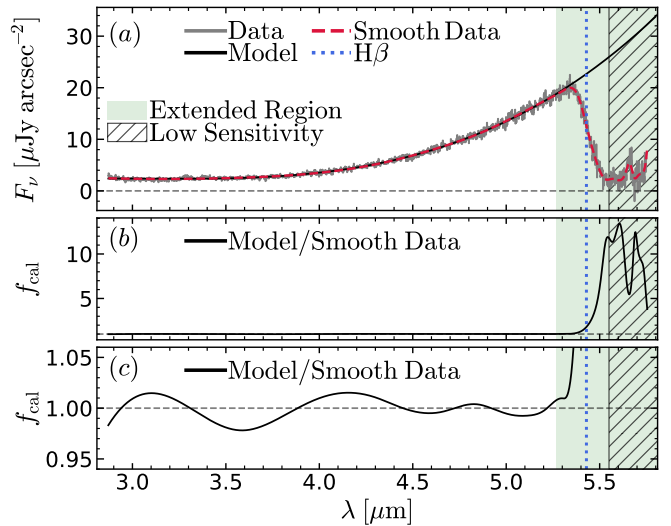


Figure 3. In Fig. 3a we display the raw and smoothed spectra from the circular aperture discussed in the main text in Section 3.2, together with the extrapolation towards longer wavelengths, outside the nominal wavelength range, but where the detector is still sensitive enough for us to extract meaningful data. Fig. 3b illustrates the variation of the derived flux calibration factor f_{cal} across the wavelength range; we zoom in to $f_{\text{cal}} \sim 1$ in Fig. 3c.

region $\lambda < 5.27 \mu\text{m}$ to model the background (black line), and to derive an extended flux-calibration term f_{cal} , the ratio between the extrapolated model background and the smoothed data. This additional term rises rapidly at $\lambda \gtrsim 5.35 \mu\text{m}$ (as shown in Fig. 3c), while at $\lambda \lesssim 5.27 \mu\text{m}$ it oscillates between 1 ± 0.02 (Fig. 3b). We consider the latter oscillations as artefacts of our background model; hence, our additional flux-calibration term is equal to unity at $\lambda \lesssim 5.27 \mu\text{m}$, and is equal to the derived f_{cal} at $\lambda > 5.27 \mu\text{m}$.

3 ANALYSIS

3.1 PSF matching for individual spaxels spectra

In the case of individual spaxels ($0.05'' \times 0.05''$) it is crucial to take into account the size of the point-spread function (PSF) of NIRSpec/IFU. We assume the PSF to be a 2-dimensional Gaussian, allowing for the observed asymmetry in the directions along and perpendicular to the IFU slices. The first such determination of the NIRSpec/IFU PSF size was performed by D’Eugenio et al. (2024a) using three different methods yielding consistent results. The authors report that the major axis of the 2-dimensional PSF is preferentially aligned with the cross-dispersion direction (the long dimension of the slices). However, we can estimate the expected axial ratio of the PSF using the parametrisation equations 3 and 4 from D’Eugenio et al. (2024a). We obtain that, for our wavelength range of interest $4 \mu\text{m} < \lambda_{\text{obs}} < 5.3 \mu\text{m}$, the difference between the PSF sizes along and perpendicular to the direction of the slicers is less than 10%. It is, therefore, reasonable to approximate the PSF shape as being circular with the FWHM given by the geometric mean between the PSF FWHM values along and across the slicers.

In a more recent work, Jones et al. (2025a) compared the wavelength-dependent PSF FWHM predicted by STPSF software²

² <https://stpsf.readthedocs.io/en/latest/>

with PSF sizes estimates based on observations of two M-type stars and one white dwarf star in calibration programmes, as well as point-like quasi-stellar objects (QSOs) from Marshall et al. (2023) and Marshall et al. (2025b). Jones et al. (2025a) obtain a good agreement between these sets of measurements and the STPSF calculations. Consequently, we will use the PSF sizes determined by STPSF throughout our analysis. The emission line with the longest wavelength in our study is H β , and the PSF FWHM at this observed wavelength ($\sim 5.43 \mu\text{m}$) is $0.22''$. Thus, we chose to PSF-match our spectra to $\text{FWHM}_{\text{PSF,max}} = 0.22''$ ($\sigma_{\text{PSF,max}} = 0.093''$). First, we retrieve the PSF sizes at all wavelengths in our datacube, $\sigma_{\text{PSF}}(\lambda)$. The parametrisation we used was obtained by fitting the same functional form for $\sigma_{\text{PSF}}(\lambda)$ as D'Eugenio et al. (2024a):

$$\sigma_{\text{PSF}} [\text{arcsec}] = 0.076 + 0.013 \times \lambda [\mu\text{m}] \times \exp(-7.6/\lambda [\mu\text{m}]). \quad (1)$$

At each wavelength, we construct a 2-dimensional circular Gaussian kernel $\mathcal{K}(\lambda)$ with a dispersion $\sigma_{\mathcal{K}}(\lambda) = \sqrt{\sigma_{\text{PSF,max}}^2 - \sigma_{\text{PSF}}^2(\lambda)}$. We convolve the collapsed images of the data cube at each wavelength λ with $\mathcal{K}(\lambda)$ and the collapsed variance datacube slices with $\mathcal{K}^2(\lambda)$ using the CONVOLVE_FFT routine from *Astropy*.

3.2 Emission lines fitting procedure

We consider a square aperture of $0.7'' \times 0.7''$ centred on the H γ emission centroid and we fit only the spaxels inside this aperture. This aperture contains most of the stellar continuum light (as shown in Fig. 1), and the fluxes of key rest-frame optical lines (as shown in Fig. A1). We do not correct for aperture losses, as we estimate them to be $\lesssim 10\%$ at $\lambda_{\text{obs}} \sim 4 - 5 \mu\text{m}$. This expectation is based on the calculations of Rodríguez Del Pino et al. (2026), for a circular aperture of radius $r \sim 0.4''$, which is comparable to the half-width of our square aperture and larger than the PSF FWHM at these wavelengths ($0.21 - 0.22''$ as argued in Section 3.1). We show the aperture spectrum in Fig. 4a, covering the wavelength range of $3600 \text{ \AA} < \lambda_{\text{rest}} < 4700 \text{ \AA}$. The key emission lines that we study are the [O II] $\lambda\lambda 3726, 3729$ doublet, the [Ne III] $\lambda\lambda 3869, 3968$ doublet, H δ , H γ , the [O III] $\lambda 4363$ auroral line and H β (see details of how it was extracted in Section 2.5). H η is not detected, which is expected, given the high order of this Balmer transition. H ζ and He I $\lambda 3889$ are blended and thus we perform a crude de-blending by adopting a truncated Gaussian prior on the H δ /H ζ ratio. The prior is centred on the case-B value of $H\delta/H\zeta = 2.46$ computed using PYNEB (Luridiana et al. 2015). This is a reasonable assumption because the system does not have significant dust attenuation (as discussed in Section 4.3). We choose a standard deviation of 0.3 for this Gaussian prior, because it is sufficiently broad to account for our most pessimistic estimates of the flux calibration uncertainties ($\sim 10\% - 15\%$). We selected H δ as it is the closest Balmer line to H ζ that is not blended. [Ne III] $\lambda 3968$ and He ϵ are blended, but we can retrieve their fluxes by fixing $[\text{Ne III}] \lambda 3968 / [\text{Ne III}] \lambda 3869 = 0.301$ (e.g., Jones et al. 2024a; Tripodi et al. 2024). All emission lines are fitted with a Gaussian; we tie the kinematics (centroid and intrinsic dispersion) of all lines. We fit the emission lines from [O II] $\lambda\lambda 3726, 3729$ to [O III] $\lambda 4363$. We clip and mask $> 3\sigma$ outliers (in line free spectral regions) in the aperture and spaxel spectra, using the SIGMA_CLIP procedure from ASTROPY (Astropy Collaboration et al. 2022).

We explored several parameterisations for the underlying continuum, including low-order polynomials and power-law models, but found strong degeneracies among the parameters governing the continuum shape in these approaches. These issues are avoided by adopting a PPIX (Cappellari 2017, 2023) fit for the continuum. In our work,

we used templates built using *FSPS* v3.2 templates³ (Conroy et al. 2009; Conroy & Gunn 2010), with the *MILES* stellar library for the optical region (Sánchez-Blázquez et al. 2006; Falcón-Barroso et al. 2011) and with the *MIST* isochrones (Choi et al. 2016). We adopted a Chabrier (2003) IMF. During the continuum fitting, spectral regions within $\pm 10 \text{ \AA}$ of the rest-frame wavelength of the main emission lines indicated in Fig. 4 were masked to prevent nebular emission from biasing the stellar continuum and absorption modelling. The continuum was fitted in the unmasked regions using both stellar and gas templates; the latter were kept enabled in order to account for possible residual contributions from faint nebular lines not included in the main emission-line mask. It is, however, important to note that the stellar continuum in our data is intrinsically very weak, and as a result the continuum fit does not strongly constrain detailed stellar population properties. Consistent with this, the underlying stellar Balmer absorption features are found to be modest: in the full-aperture spectrum we measured the rest-frame equivalent widths of $\text{EW}(\text{H}\gamma) \approx 0.36 \text{ \AA}$ and $\text{EW}(\text{H}\delta) \approx 0.57 \text{ \AA}$ in the best-fit stellar model. These imply that the uncertainties in the modelling of the continuum and stellar absorption features have a negligible impact on the emission line fluxes (calculated at a later step), which represent the core part of our analysis.

To take into account the possible systematics in the errors measured within the pipeline, we re-scaled the nominal flux uncertainties (extracted from the datacube ‘ERR’ extension file) such that the median value of the noise in a given spaxel (across the wavelength slices free of emission lines) matches the standard deviation of the residuals from the spectrum fit in the spectral regions free of emission lines. Because the noise re-scaling factor is not known beforehand, we allowed it to be a free parameter of our fitting algorithms. A similar noise re-scaling approach was implemented by Jones et al. (2025b) in the case of their study of a $z \sim 4.26$ rotating disc star forming galaxy. For individual spaxels, re-scaling factors vary between 1.9 and 2.5 (Übler et al. 2023, 2024; Venturi et al. 2025). Finally, in the case of aperture spectra (obtained by adding the spectra of individual spaxels within them), we obtain the uncertainties by adding in quadrature the re-scaled uncertainties in the spaxels spectra.

We first identify a minimum χ^2 solution of our emission line fitting algorithm by using a least squares procedure. In order to de-convolve the intrinsic line profiles from the observed features, we assume that the wavelength-dependent line spread function (LSF) of NIRSpec is given by the nominal, pre-launch resolution $\text{FWHM}_{\text{LSF pre-launch}}$ (Jakobsen et al. 2022) – assumed to be Gaussian – improved by a factor 0.8, following Shajib et al. (2025, and roughly in agreement with e.g., Greene et al. 2024). The pre-launch estimates for the LSF width were too conservative because the *JWST* provides a lower than expected wavefront error. The intrinsic $\text{FWHM}_{\text{intr}}$ is thus:

$$\text{FWHM}_{\text{intr}} = \sqrt{\text{FWHM}_{\text{obs}}^2 - (0.8 \times \text{FWHM}_{\text{LSF pre-launch}})^2}. \quad (2)$$

After this step, we use the least-squares solution to initialise the chains for computing the posterior distribution of our models using a Markov chain Monte Carlo (MCMC) method and the software EMCEE (Foreman-Mackey et al. 2013). The fiducial parameters are the median values of the marginalised posterior distributions over each parameter and the uncertainties are derived from the 16th and 84th percentiles. We assumed flat priors on all of the parameters and we set the following prior bounds: $0 < \log(F_{\text{int}}/10^{-20} \text{ erg s}^{-1} \text{ cm}^{-2}) < 3$ for integrated fluxes, $10.15 < z < 10.20$ and $100 \text{ km s}^{-1} < \text{FWHM} <$

³ <https://github.com/cconroy20/fsps>

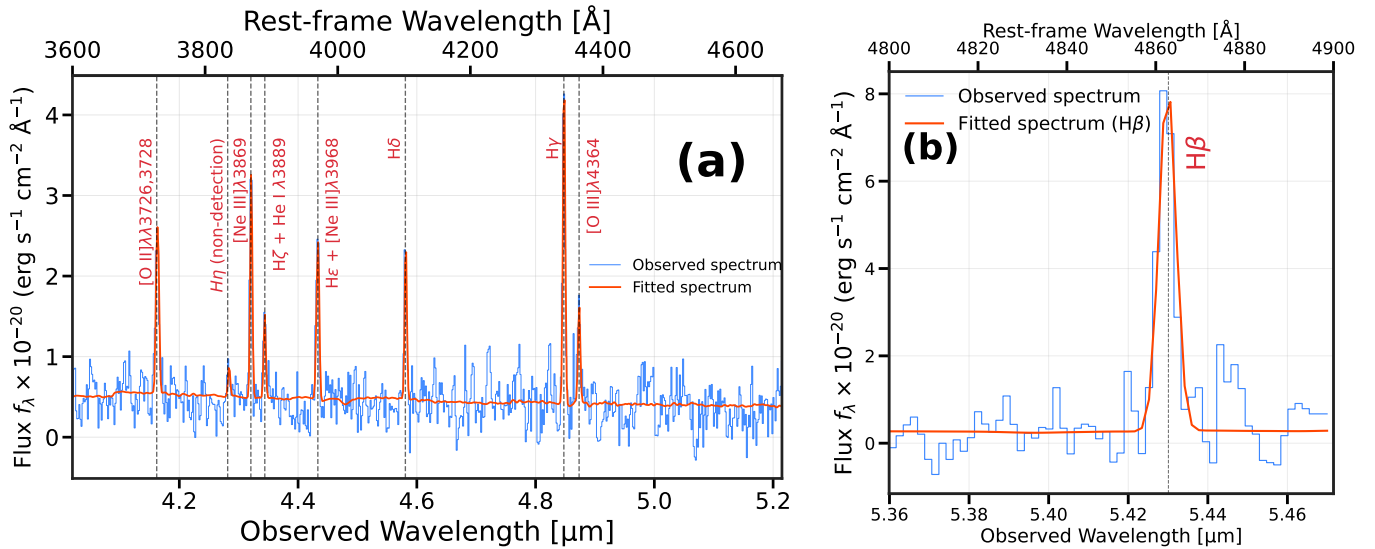


Figure 4. Fig. 4a shows the observed integrated aperture spectrum in the rest-frame wavelength range between 3600 Å and 4700 Å, highlighting the key emission lines discussed in the main text, including the [O II] doublet and blended features. Fig. 4b represents a zoom-in over the spectral wavelength range $4800 \text{ \AA} < \lambda_{\text{rest}} < 4900 \text{ \AA}$, which, for $z = 10.17$, is redder than the nominal wavelength coverage of NIRSpec/G395M (2.87 – 5.27 μm). The plot highlights the best-fit of the H β line assuming only one Gaussian component, constrained by the kinematics of multiple emission lines shown in the left panel.

500 km s^{-1} . For the ratio [O II] $\lambda 3729$ /[O II] $\lambda 3726$ we assume a range of [0.34; 1.5] (Sanders et al. 2016). We furthermore fitted the two [O II] $\lambda 3726, 3729$ doublet components individually and tied their kinematics to those of other features (included non-blended features). We note that, even though we fitted the [O II] $\lambda 3726, 3729$ doublet components individually and tie their kinematics to those of other, non-blended features, our medium-resolution data cannot fully break the degeneracy between the red-to-blue line ratio [O II] $\lambda 3729$ /[O II] $\lambda 3726$ and the flux of the blue component. However, the total [O II] $\lambda 3726, 3729$ flux is well constrained and we will focus on this parameter from now onwards.

Additionally, we tested an alternative fitting model for the integrated aperture-spectrum where we assumed that all emission lines are fitted by two Gaussians from two sets of kinematically tied components (but the broader Gaussians are allowed to vary between $100 \text{ km s}^{-1} < \text{FWHM} < 1000 \text{ km s}^{-1}$). However, a simple Bayesian Information Criterion (BIC; Schwarz 1978) test finds that $\Delta\text{BIC} \equiv \text{BIC}_{2 \text{ comp}} - \text{BIC}_{1 \text{ comp}} \approx 11$. Hence, the 2-Gaussians model is statistically disfavoured over the single Gaussian model (even in the high S/N aperture spectrum). We repeated this analysis for the spaxel spectra in the wavelength range $3600 \text{ \AA} < \lambda_{\text{rest}} < 4700 \text{ \AA}$, but concluded that no spaxel simultaneously satisfied both the conditions that $\Delta\text{BIC} < -10$ (this condition would mean that a fit with two components is statistically favoured) and $\text{S/N} > 3$ for the secondary, high-FWHM component. Therefore, it is reasonable to adopt single Gaussian fits for all spaxels. In the case of the H β , this is fitted separately from other rest-frame optical emission lines, given the higher uncertainties of the continuum at $\lambda_{\text{obs}} > 5.27 \mu\text{m}$ outside the nominal range covered by G395M/F290LP. The kinematics of H β were tied to the lower-wavelength lines, by imposing the posteriors of redshift and FWHM (derived from our $3600 \text{ \AA} < \lambda_{\text{rest}} < 4700 \text{ \AA}$ emission lines fit) as the priors of the H β redshift and FWHM. This approach further allows some flexibility in deriving the H β kinematics and accounts better for possible wavelength calibration uncertainties than simply fixing $z_{\text{H}\beta}$ and $\text{FWHM}_{\text{H}\beta}$ to the median values of the posterior distributions from the $3600 \text{ \AA} < \lambda_{\text{rest}} < 4700 \text{ \AA}$ fit. Only the H β flux was fitted as a free parameter with a flat prior distribution.

Following these methods, we obtain the integrated aperture spectra over the $3600 \text{ \AA} < \lambda_{\text{rest}} < 4700 \text{ \AA}$ wavelength range (Fig. 4a) and in the spectral region around H β (Fig. 4b). The latter allows us to estimate the uncertainties in our flux calibration outside the nominal wavelength range of the G395M/F290LP setup. We estimate an integrated H β flux of $(3.69 \pm 0.23) \times 10^{-18} \text{ erg s}^{-1} \text{ cm}^{-2}$ from the spectrum of the full aperture (shown in Fig. 4b). Hsiao et al. (2024b) present MIRI MRS IFU observations of the MACS0647-JD1 lensed image of our target but do not detect H β directly. The authors estimate an H β flux of $(3.29 \pm 0.37) \times 10^{-18} \text{ erg s}^{-1} \text{ cm}^{-2}$ by extrapolating based on the detected H α flux of $(9 \pm 1) \times 10^{-18} \text{ erg s}^{-1} \text{ cm}^{-2}$ and assuming a case-B ratio of $H\alpha/H\beta \sim 2.74$ at $T_e = 20000 \text{ K}$. While it is possible that there is a small quantity of dust in the system, it would have a much smaller effect on changing the inferred H β flux, compared to the errorbars on the flux measurement itself (as we argue in more detail in Section 4.3). We therefore conclude that within the associated uncertainties, the H β flux inferred by Hsiao et al. (2024b) is consistent with full-aperture H β flux in our data-cube, which suggests that the flux calibration uncertainties in the extended spectral region of the data-cube are less than $\sim 15\%$.

Using the same methods described above, we obtained the line ratios maps for $\text{O3H}\gamma \equiv \log([\text{O III}] \lambda 4363/\text{H}\gamma)$ and $\text{Ne3O2} \equiv \log([\text{Ne III}] \lambda 3869/[\text{O II}] \lambda 3726, 3729)$. These are displayed in Fig. 5a and Fig. 5b, together with the gas FWHM map, in Fig. 5d.

3.3 Combined SED fitting of photometry and spectroscopy

To study the link between the spatially resolved ISM properties and star-formation histories, we measure the stellar-population properties of the MACS0647-JD system using PROSPECTOR, a Bayesian SED modelling tool (Johnson et al. 2021), built around the Flexible Stellar Population Synthesis (FSPS; Conroy et al. 2009; Conroy & Gunn 2010) tool. We fit the NIRCcam photometry and NIRSpec/G395M spectroscopy of MACS0647-JD1 simultaneously for all spaxels in the cutout described in Section 3.2. We use the MILES stellar spectral library (Sánchez-Blázquez et al. 2006; Falcón-Barroso et al. 2011) and the MIST isochrones (Choi et al. 2016). Our stellar mass

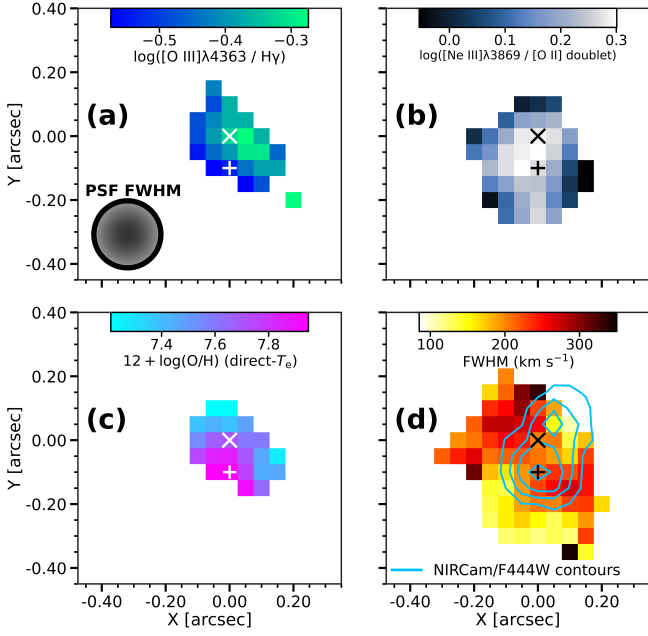


Figure 5. **Top panels:** maps of the diagnostic ratios O3Hg and Ne3O2 (allowing only spaxels with $S/N > 3$ for each emission line involved). **The bottom panels** show the spaxel-by-spaxel maps of gas-phase metallicity (Fig. 5c; showing only the spaxels with $S/N > 3$ for $[\text{O III}]\lambda 4363$, $\text{H}\gamma$ and inferred $[\text{O III}]\lambda 5007$) and the intrinsic, de-convolved gas FWHM (Fig. 5d; we only show spaxels with a $S/N > 5$ detection of $\text{H}\gamma$). The FWHM map shows two high-dispersion regions which coincide with the locations of the metal-poor gas. The ‘x’ and ‘+’ crosses mark the $\text{H}\gamma$ emission-line and the F444W stellar continuum centroids, respectively (as in Fig. 2). We also show the PSF size on the top left panel for comparison.

prior is informed by the observed stellar mass function, and the composite stellar populations are constructed as in the PROSPECTOR- β model (Wang et al. 2023a). The stellar metallicity follows a truncated Gaussian prior $\log(Z_*/Z_\odot) \sim \mathcal{N}(-1.0; 0.5)$, truncated to $[-2.0; 0.0]$. We adopt a flexible non-parametric SFH continuity prior (Leja et al. 2019) with eight age bins. Nebular emission is modelled using CLOUDY (v13.03, Ferland et al. 2013, 2017) as implemented in FSPS (Byler et al. 2017). The dust attenuation is modelled using the two-component model of Charlot & Fall (2000), with a diffuse dust component optical depth $\tau_2 \sim \mathcal{N}(0.3; 1)$, truncated to $[0; 4]$, and a birth-cloud-to-diffuse dust ratio $\tau_1/\tau_2 \sim \mathcal{N}(1; 0.3)$, truncated to $[0; 2]$. The attenuation curve slope n_{dust} is drawn from a uniform prior over $[-1.2; 0.4]$ (Noll et al. 2009). We do not include dust emission in our model, as it is negligible at the rest-frame wavelengths $\lesssim 5000 \text{ \AA}$ that we probe. We also account for absorption due to the intergalactic medium following the prescription of Inoue et al. (2014). To account for flux calibration and slit-loss effects, we model the spectral response using an eighth-order polynomial distortion that allows the observed spectrum to match the continuum shape predicted by the SED model. We additionally include a single ‘jitter’ parameter that rescales the spectral uncertainties, capturing residual calibration systematics and ensuring a statistically consistent fit.

We present our results in Section 5.1.4 where we discuss the implications of the spatial distribution of the stellar mass and of star formation burstiness (defined as $\text{SFR}_{10}/\text{SFR}_{100}$, the ratio of the star formation rates averaged on lookback timescales of 10 and 100 Myr, respectively) within the system. We report the star formation histories and the corner plot showing the posterior distributions and

Table 1. Physical parameters of the MACS0647-JD1 system and of its main stellar components. The top rows in this table present our results for some properties derived directly from large integrated aperture spectra and from the spectra corresponding to the SE and NW clumps. The bottom rows, on the other hand, give the values of various parameters resulting from spectro-photometric SED modelling (see Section 3.3 and Section 5.1.4).

Parameter	Full Aperture	SE Clump	NW Clump
gas FWHM (km s^{-1})	228 ± 19	215 ± 34	189 ± 41
$12 + \log(\text{O}/\text{H})$ (dir)	7.59 ± 0.12	7.89 ± 0.11	7.47 ± 0.14
$12 + \log(\text{O}/\text{H})$ (str)	7.66 ± 0.08	7.71 ± 0.08	7.49 ± 0.09
T_e $[\text{O III}]/10^4 \text{ K}$	1.90 ± 0.25	1.52 ± 0.21	$2.38^{+0.25}_{-0.34}$
$\log U$	-2.05 ± 0.07	-1.84 ± 0.06	-1.84 ± 0.09
$\text{SFR}_{\text{H}\gamma}$ ($M_\odot \text{ yr}^{-1}$)	5.5 ± 1.0	1.0 ± 0.2	0.50 ± 0.15
SFR_{100} ($M_\odot \text{ yr}^{-1}$)	2.9 ± 0.4	0.56 ± 0.10	0.24 ± 0.05
$\log(M_*/M_\odot)$	8.38 ± 0.21	7.78 ± 0.07	7.41 ± 0.08
$A_{V,\text{cont}}$ (PROSPECTOR)	0.26 ± 0.15	0.13 ± 0.05	0.18 ± 0.07

the correlations between various SED parameters in the case of the two main stellar components (Fig. D1 and Fig. D2 in Appendix D).

4 RESULTS

4.1 Direct-method gas-phase metallicities

To calculate the electron temperatures from the spectra of individual spaxels (required to infer the direct- T_e metallicities), we need to infer the $[\text{O III}]\lambda 5007$ fluxes. We use equation (1) from Witstok et al. (2021), which connects the observed $[\text{O III}]\lambda 5007 / [\text{O II}]\lambda\lambda 3726, 3729$ and $[\text{Ne III}]\lambda 3869 / [\text{O II}]\lambda\lambda 3726, 3729$ ratios for star forming galaxies:

$$\log\left(\frac{[\text{O III}]\lambda 5007}{[\text{O II}]\lambda\lambda 3726, 3729}\right) = 0.905 \log\left(\frac{[\text{Ne III}]\lambda 3869}{[\text{O II}]\lambda\lambda 3726, 3729}\right) + 1.078. \quad (3)$$

This method of estimating the flux of $[\text{O III}]\lambda 5007$ was also used by several works studying the physical properties of the ISM (metallicity, ionisation parameter) in $z > 10$ galaxies (Bunker et al. 2023; Scholtz et al. 2025a). For the integrated-aperture spectrum of MACS0647-JD1, the inferred $[\text{O III}]\lambda 5007$ integrated line flux is $(2.24 \pm 0.48) \times 10^{-17} \text{ erg s}^{-1} \text{ cm}^{-2}$, consistent with the value of Hsiao et al. (2024b) from MIRI medium-resolution spectroscopy, demonstrating the potential of the method proposed by Witstok et al. (2021) to extrapolate $[\text{O III}]\lambda 5007$ based on $[\text{Ne III}]\lambda 3869$ at $z > 10$, where $[\text{O III}]\lambda 5007$ falls outside the wavelength range of NIRSPEC. Although the empirical equation 3 was derived based on $z \sim 0$ galaxies from SDSS, such a correlation between $[\text{O III}]\lambda 5007 / [\text{O II}]\lambda\lambda 3726, 3729$ and $[\text{Ne III}]\lambda 3869 / [\text{O II}]\lambda\lambda 3726, 3729$ has been recently shown to exist at least up to $z \sim 9.5$, as illustrated by the figure 6 of Zamora et al. (2025a), based on a compilation of $z > 5$ JWST observations (Arellano-Córdova et al. 2022; Cameron et al. 2023; Curti et al. 2023; Sanders et al. 2023a; Heintz et al. 2024; Schaerer et al. 2024; Topping et al. 2024; Curti et al. 2025).

The ‘direct’ electron temperature is calculated using $[\text{O III}]\lambda 4363 / [\text{O III}]\lambda 5007$. We assume, at first, that the dust attenuation is negligible ($A_{V,\text{cont}} \lesssim 0.1 \text{ mag}$; Hsiao et al. 2024a). For the full aperture spectrum, PYNEB (Luridiana et al. 2015) predicts a mean temperature of the $[\text{O III}]\lambda 5007$ emitting gas region $T_e[\text{O III}] = (1.9 \pm 0.3) \times 10^4 \text{ K}$ for an auroral-to-strong ratio of 0.031 ± 0.008 , assuming an electron density of 2000 cm^{-3} (as determined by Abdurro’uf et al. 2024 using high-resolution spectroscopic

data for our target). We also tested a wide range of electron densities $100 \text{ cm}^{-3} < n_e < 10000 \text{ cm}^{-3}$ which extends more than the typical range of electron densities in high-redshift galaxies (Isobe et al. 2023b; Marconcini et al. 2024; Scholtz et al. 2025b) and we found that the dependence of our T_e [O III] estimate on the assumed n_e is negligible. A similar procedure is applied for computing the electron temperatures from individual spaxel spectra, and our results are displayed in Fig. 7b. Once we calculate our T_e [O III] values, we can calculate the electron temperature of the [O II] emitting gas using equation (14) from Izotov et al. (2006). We can then compute the gas-phase metallicities (as given by oxygen abundances). Dors et al. (2020) showed that the contribution of O^{3+} is negligible even in highly AGN-dominated regimes. Thus, we can assume all oxygen atoms are either singly or doubly ionised in these conditions. We use [O II] $\lambda\lambda 3726, 3729/H\beta$ and [O III] $\lambda 5007/H\beta$ to compute the abundances of the O^+ and O^{++} ions using PYNEB. For the aperture spectrum, we obtain $12 + \log(\text{O}/\text{H}) = 7.59 \pm 0.12$, in agreement with the result of Hsiao et al. (2024b) and also similar to the direct- T_e metallicities reported for a number of other SFGs at $z \sim 4 - 9$ (e.g., Curti et al. 2023; Heintz et al. 2023; Nakajima et al. 2023; Morishita et al. 2024). In order to additionally test for consistency (given the indirect method used for extracting $H\beta$ fluxes), we repeat our calculation but this time we use the ratios [O II] $\lambda\lambda 3726, 3729/H\gamma$ and [O III] $\lambda 5007/H\gamma$ (instead of their counterparts involving $H\beta$). We obtain $12 + \log(\text{O}/\text{H}) = 7.52 \pm 0.13$ in agreement with our previous value, and acting as a cross-validation of both the method and the flux calibration. For individual spaxels, we additionally perform the dust attenuation corrections described in Section 4.3. The resulting metallicity map is shown in Fig. 5c.

To assess the impact of dust reddening on our calculated parameters, we adopted a stellar continuum dust attenuation following the Calzetti law (Calzetti et al. 2000) with $A_{V,\text{cont}} = 1$ mag for the full-aperture spectrum (albeit unreasonably high from a physical point of view; Ferrara et al. 2025). This would imply a gas-phase metallicity of $12 + \log(\text{O}/\text{H}) = 7.71$, which is within the quoted uncertainties of our $A_{V,\text{cont}} = 0$ estimate. For an assumed $A_{V,\text{cont}} = 2$ mag, we obtain $12 + \log(\text{O}/\text{H}) = 7.90$. Thus, as a first-order approximation, the change in calculated metallicity and that in assumed dust attenuation are related by: $\Delta \log(\text{O}/\text{H}) / \Delta A_{V,\text{cont}} \approx 0.18 \text{ dex mag}^{-1}$.

4.2 Identification of AGN dominated spaxels

To constrain the dominating ISM excitation mechanism, we use the star-forming/AGN diagnostic diagram from Mazzolari et al. (2024) which can classify spectra as AGN only, or consistent with both AGN and star formation. These diagnostics are commonly used in studying high-redshift AGN (e.g., Juodžbalis et al. 2025; Mazzolari et al. 2025; Geris et al. 2026; Ivey et al. 2026). We focus on the emission line ratios O3Hg and Ne3O2. According to equation (5) from Mazzolari et al. (2024), the ‘AGN-only’ scenario is disfavoured for the integrated spectrum of MACS0647-JD1 and the SE clump, but it is consistent within the 1σ uncertainties for the NW clump. A number of spaxels in the south-west region are identified as AGN dominated (above the demarcation line from Fig. 6b) and some are below the demarcation line, but still close to it (Fig. 6a). Given the large error bars, and given the predominant location of ‘AGN-only’ spaxels away from the centre, we disfavour an AGN interpretation.

Supporting this interpretation, no spaxel is identified as purely dominated by AGN if we alternatively use the O3Hg vs O32 or O3Hg vs O33 ($\equiv \log([\text{O III}] \lambda 5007 / [\text{O III}] \lambda 4363)$) diagnostics (as shown in Fig. B1 in Appendix B). However, in this case, the uncertainties are larger than for the previous diagram, given that: *i*) both the O32

and O33 ratios require a reddening correction, and *ii*) our spatially resolved [O III] $\lambda 5007$ fluxes are obtained using the extrapolation method described in Section 4.1. In summary, while we disfavour an AGN interpretation, we provide a cautionary note regarding the interpretation of strong-line metallicities in this south-western region.

4.3 Dust attenuation corrections

Various recent studies use the Balmer decrement ratios to compute the nebular dust attenuation for individual spaxels (Venturi et al. 2024; Ivey et al. 2026). In our case, thanks to our custom $H\beta$ extraction procedure (Section 2.5), the lowest order Balmer lines are $H\beta$ and $H\gamma$. We use PYNEB to compute the theoretical case-B Balmer ratio $(H\beta/H\gamma)_0 = 2.105$ (assuming $T_e = 19000 \text{ K}$ as derived in Section 4.1). The stellar continuum dust attenuation is:

$$A_{V,\text{cont}} = -2.5 \times 0.44 \times \log(\phi_{\text{obs}}/\phi_0) \times R_V / (k_{\lambda,H\beta} - k_{\lambda,H\gamma}), \quad (4)$$

where the factor of 0.44 comes from the relation between stellar and nebular dust attenuation (Calzetti et al. 2000) and we define $\phi \equiv H\beta/H\gamma$. We assume $R_V = 4.05$ (Calzetti et al. 2000). For the dust attenuation law, we assume a slightly modified version of the Calzetti law that is suitable for low-mass, low-metallicity galaxies (Shivaei et al. 2020). We obtain that, for all the spaxels considered in computing the direct method metallicity map, except for three outliers, $A_{V,\text{cont}} \lesssim 0.3$ mag (and consistent with 0 within the uncertainties) whereas the highest outlier has $A_{V,\text{cont}} \approx 0.6$ mag. According to our previously calculated $\Delta \log(\text{O}/\text{H}) / \Delta A_{V,\text{cont}} \approx 0.18 \text{ dex mag}^{-1}$ (Section 4.1), it means that the effect of dust attenuation correction on the derived spaxels metallicities is less than 0.11 dex. We will therefore, as a first-order approximation, correct the line ratios from spaxels spectra assuming the Calzetti dust attenuation curve with the $A_{V,\text{cont}}$ derived using this method.

We now separately discuss the cases of individual spaxels with $H\beta/H\gamma < (H\beta/H\gamma)_0$ (which cannot be explained by dust attenuation assuming case B recombination). In all but four cases of spaxels with below case-B $H\beta/H\gamma$ decrement ratios and $S/N > 3$ on all $H\beta$, $H\gamma$ and $H\delta$, we notice that the $H\gamma/H\delta$ remains above the corresponding case-B Balmer ratio. In principle, higher stellar absorption in $H\beta$ could be responsible for such a behaviour (Groves et al. 2012; Tacchella et al. 2023); while our PPIX continuum modelling allows for stellar absorption (as described in Section 3.2), the weakness of the continuum of our $z \sim 10.17$ target implies that any stellar absorption has a negligible impact on the measured fluxes of the emission lines. Moreover, potential calibration uncertainties in the extrapolated wavelength range ($\lambda_{\text{obs}} > 5.27 \mu\text{m}$) could also contribute to artificially low $H\beta$ fluxes. Due to the wavelength proximity of $H\gamma/H\delta$, this ratio is not suitable to accurately calculate the dust attenuation, especially in low S/N targets. As a result, we assume that $A_{V,\text{cont}} = 0$ mag for these spaxels.

There are only four spaxels for which both $H\beta/H\gamma$ and $H\gamma/H\delta$ are more than 1σ below their expected case-B values and all are located westwards of the south-east clump, in the region for which we expect some non-negligible contribution from AGN (as discussed in Section 4.2). Indeed, below case-B Balmer ratios $H\beta/H\gamma$ (and $H\alpha/H\beta$) have been reported for stacked Type-2 AGN (Scholtz et al. 2025c). Case-B assumptions may not be fulfilled in cases of optically thin or non-equilibrium conditions (Scarlatà et al. 2024). While such conditions typically require high electron temperatures and/or low electron densities, which are not indicated by our measurements, we cannot exclude localised departures from Case-B assumptions in these regions. We adopt a similar approach of assuming $A_{V,\text{cont}} = 0$ mag for

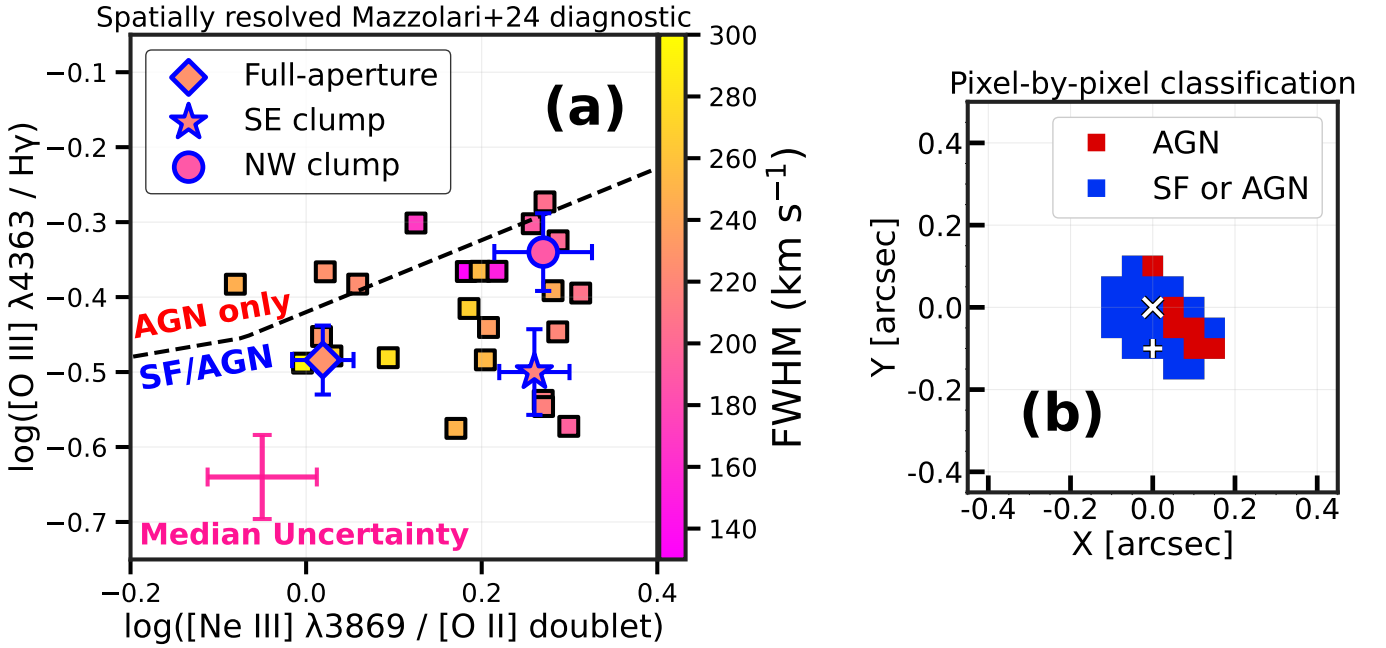


Figure 6. Fig. 6a illustrates the position of individual spaxels on the O3H γ vs Ne3O2 diagnostic diagram from Mazzolari et al. (2024). The dashed demarcation line separates regimes that are fully dominated by AGN photoionisation (AGN only) from regions in which both AGN and/or star formation may have similar contributions. Squares are individual spaxels, colour coded by the FWHM from the single Gaussian component fit. We only show the pixels in which $S/N > 5$ for H γ and [Ne III] $\lambda 3869$ and $S/N > 3$ for [O III] $\lambda 4363$ and for [O II]. The pink error-bars are the median uncertainties based on spaxels measurements. The ratios from the full-aperture, NW and SE clump spectra lie below the demarcation line. On the spatially resolved map (Fig. 6b), we identify the spaxels with either AGN or SF/AGN classification.

these spaxels. We expect that this assumption has a negligible impact on the derived gas-phase metallicities, given the findings of Hsiao et al. (2024a), claiming $A_{V,cont} \lesssim 0.3$ mag for the integrated aperture spectrum (covering the south-east clump within the slit).

As an additional sanity check, we estimate $A_{V,cont}$ based on our combined spaxel-by-spaxel PROSPECTOR SED fits (described in Section 3.3). Taking into account that both diffuse dust (optical depth τ_2) and dust from the birth clouds (optical depth τ_1) contribute to the total dust attenuation, we approximate $A_{V,cont} \approx 2.5 \times 0.44 \times \log_{10}(e) \times (\tau_1 + \tau_2)$. In reality, this formula gives an upper limit on $A_{V,cont}$, with the actual value depending on the exact fraction of light coming from young stars (< 10 Myr) relative to the total, but it goes beyond the scope of this paper to constrain this parameter. From this calculation, we obtain that, in the case of spaxels with $S/N_{[O III] \lambda 4363} > 3$, the highest $A_{V,cont}$ is ~ 0.5 mag, although most spaxels have $A_{V,cont} \sim 0.0 - 0.4$ mag. The values obtained for the two clumps and for the full cutout aperture are reported in Table 1. Overall, our results obtained with these methods are in agreement, and here we illustrate the difficulty of providing accurate dust corrections on spatially resolved scales (also mentioned by Hutchison et al. 2025). However, we demonstrate that, whichever dust correction method we implement, the effect on the inferred metallicities is expected to be smaller than the measurement uncertainties.

4.4 Ionisation parameter

For the ionisation parameter, one standard approach is to use the diagnostic O32 $\equiv \log [O III] \lambda 5007 / [O II] \lambda \lambda 3726, 3729$ as these lines trace different ionisation stages of the same atom species (Díaz et al. 2000; Kewley & Dopita 2002; Papovich et al. 2022). [O III] $\lambda 5007$ is unavailable in our spectra, even despite our retrieval of spectral data

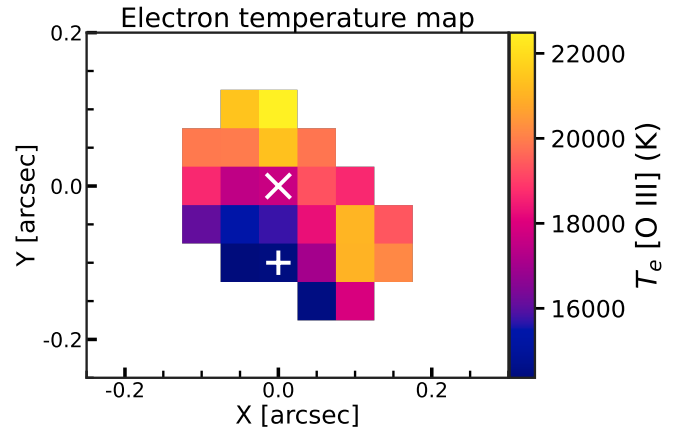


Figure 7. This figure shows the map of the electron temperature of the [O III] emitting gas in the central region of the system. We only show spaxels with $S/N > 3$ for the auroral [O III] $\lambda 4363$ line. The white ‘+’ and ‘x’ crosses mark the centroids of stellar continuum and H γ line emission, respectively.

outside the nominal range of G395M grating. As an alternative we use the Ne3O2 which closely tracks O32 and it has the advantage that the wavelengths of these lines are close to each other, so their ratio is insensitive to dust reddening (Nagao et al. 2006; Pérez-Montero et al. 2007; Levesque & Richardson 2014; Maiolino & Mannucci 2019). In order to determine the ionisation parameter, we use equation (3) from Witstok et al. (2021), based on the original equation by Díaz et al. 2000 from single-star photoionisation models).

We obtain $\log U = -2.05 \pm 0.07$ for the full aperture spectrum and $\log U = -1.84 \pm 0.06$ for both the south-east and the north-

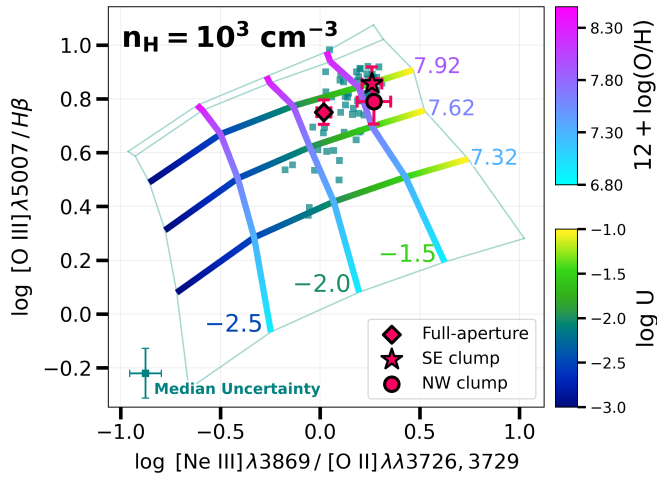


Figure 8. This figure shows the R3-Ne3O2 photoionisation grid (with varying metallicity and ionisation parameter) of SFGs from Gutkin et al. (2016) based on *CLOUDY* models (Ferland et al. 2013, 2017). The choice of the grid is motivated in the main text of Section 4.5. Individual spaxels (with $S/N > 5$ on $[\text{Ne III}] \lambda 3869$, $[\text{O II}] \lambda 3726, 3729$ and $\text{H}\beta$ lines) are plotted as dark-cyan small squares and their median uncertainties are shown in the bottom left part. Blue symbols denote the results from the full-aperture and the two main components. These two line ratios also offer the advantage that they do not require dust reddening correction.

west components, consistent with the result obtained by Hsiao et al. (2024a). The calculated $\log U$ values are somewhat higher compared to other star-forming galaxies (SFGs) at $3.5 < z < 10$ (Christensen et al. 2012; Troncoso et al. 2014; Shapley et al. 2017; Marconcini et al. 2024; Rodríguez Del Pino et al. 2024; Hayes et al. 2025; Parlanti et al. 2025b), resulting in a more intense radiation field. Our values are instead similar to other $z > 10$ galaxies such as GHZ2 (Castellano et al. 2024; Zavala et al. 2025) and GN-z11 (Bunker et al. 2023). On spatially resolved scales, Fig. 5b shows a quite uniform Ne3O2 (and, by extrapolation, $\log U$) in the central regions of MACS0647-JD1, with a radial decrease of 0.33 ± 0.14 dex from the centre of the system towards its external regions, with a pronounced low-ionisation in the south-western region, a feature possibly indicating ionisation stratification, which we will discuss in greater detail in Section 5.1.1.

4.5 Gas-phase metallicities (strong-line method)

The strong nebular emission lines provide an alternative method to estimate gas-phase metallicities in high-redshift SFGs (e.g. Nakajima et al. 2022; Curti et al. 2024; Cataldi et al. 2025; Sanders et al. 2025; Scholte et al. 2025). These calibrations are valid only for SFGs and link strong emission-line ratios with metallicities based on the more reliable and more general ‘direct’ method. However, it is important to note that these studies use integrated aperture spectra, so they do not account for spatial variations in the ISM conditions and/or physical systematics effects (e.g. localised shocks, AGN) that can impact the metallicity measurements on resolved scales. In this work, we chose to use the robust star-forming galaxies R3 vs Ne3O2 photoionisation grid from Gutkin et al. (2016) as shown in Fig. 8. We chose $R3 \equiv \log([\text{O III}] \lambda 5007 / \text{H}\beta)$ as a primary tracer of metallicity, with $[\text{O III}] \lambda 5007$ fluxes calculated based on Witstok et al. (2021) equation. To break the degeneracy with the ionisation parameter, we additionally use Ne3O2 (Maiolino & Mannucci 2019). This photoionisation grid method has the further advantage that both line

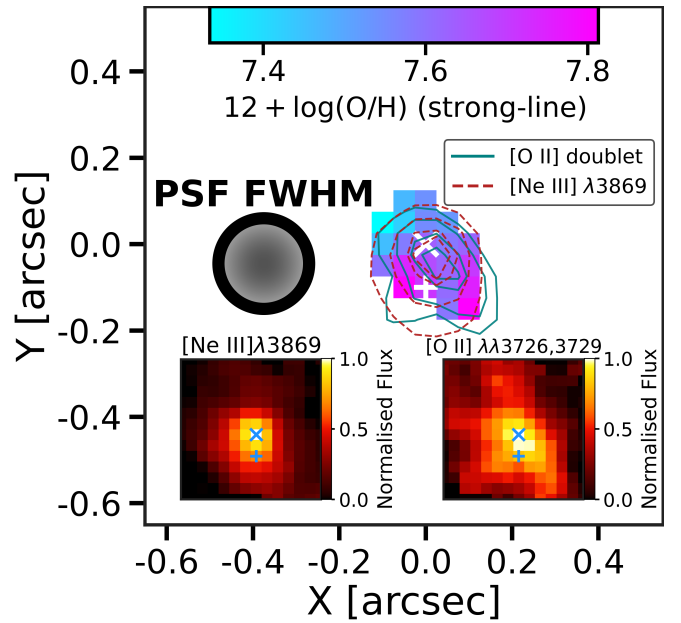


Figure 9. Metallicity map based on R3-Ne3O2 line ratios (Section 4.5). Here, we only highlight the spaxels that have $S/N > 5$ for all lines involved and additionally $S/N > 3$ for $[\text{O III}] \lambda 4363$ enabling a direct comparison to the direct method metallicity map (Fig. 5). We find excellent agreement with the direct-method, except for the south-western region; this is where line ratios show tentative evidence of photoionization influenced by other processes, in addition to star formation (such as, for example, AGN, shocks or DIG). We overplot the contours of the integrated fluxes of $[\text{O II}] \lambda \lambda 3726, 3729$ (teal) and $[\text{Ne III}] \lambda 3869$ (fire-brick). Both the contours and the inset panels show that $[\text{Ne III}]$ has a more compact distribution while $[\text{O II}]$ is more extended. The blue ‘x’ and ‘+’ crosses in the inset panels are the centroids of peak $\text{H}\gamma$ (and $[\text{Ne III}] \lambda 3869$) emission and of stellar continuum, respectively.

ratios are insensitive to dust attenuation since all the emission lines involved in our calculations have similar wavelengths.

Hsiao et al. (2025) measures a carbon abundance of $\log(C/O) = -0.44 \pm 0.07$ for MACS0647-JD1. Given the value of $(C/O)_{\odot} = 0.44$ assumed by Gutkin et al. (2016), we select the grid with a carbon abundance of $(C/O) = 0.72 (C/O)_{\odot}$ which is the closest available value to the value of $0.82^{+0.13}_{-0.09} (C/O)_{\odot}$ measured by Hsiao et al. (2025). We choose an upper stellar mass cutoff for the IMF to be $100 M_{\odot}$ for our grid and a fiducial hydrogen gas density of $n_H = 10^3 \text{ cm}^{-3}$, similar to the average electron density reported by Abdurro’uf et al. (2024) for this system. However, no significant changes in the grid positions occur even if we choose $n_H = 10^2$ or 10^4 cm^{-3} . We assume a low dust-to-metal mass ratio of $\xi_d = 0.1$ which is suitable for $z > 10$ galaxies (Ferrara et al. 2025). The results are shown in Fig. 9, where we showed the positions on the chosen photoionisation grid of individual spaxels spectra. In order to convert from Z_{\odot} to oxygen abundance units, we use $12 + \log(O/H) = 8.80 + \log(Z/Z_{\odot})$ where 8.80 is the solar oxygen abundance computed by Gutkin et al. (2016) for $\xi_d = 0.1$.

5 DISCUSSION

5.1 The nature of the MACS0647-JD system

5.1.1 Emission lines spatial distribution

To characterise the morphology of the ISM within the MACS0647-JD1 system, we first identify the brightest spaxel in the emission-line

maps of H γ and [Ne III] λ 3869. This is shifted by two spaxels (corresponding to a physical, de-lensed distance of ~ 150 pc, as shown in Fig. 2) relative to the centroid of the synthetic F444W image obtained by convolving the datacube with the response function of the NIRCcam/F444W bandpass. Such a shift could arise from differential dust attenuation between the emission lines and the stellar continuum. However, MACS0647-JD is dust poor (as shown in Section 4.3 and Hsiao et al. 2024a), making this possibility unlikely. Thus, the observed offset likely implies a different spatial distribution of the line-emitting gas relative to the stars. Since the instantaneous SFR is directly responsible for the strength of the Balmer lines (Kennicutt & Evans 2012), it means that the central region between the two stellar clumps (Fig. 2b) hosts the most intense recent star-formation activity, while the two stellar components are dominated by older stellar populations. This could favour a merger scenario for this system, in agreement with the findings of Duan et al. (2024) and Puskás et al. (2025a) who report that, on average, high-redshift mergers trigger short-lived star formation enhancements if the components become separated by a proper distance of less than 20 kpc.

There is a striking difference in the spatial distribution of the [O II] λ 3726, 3729 compared to [Ne III] λ 3869 emission. The latter is definitely a reasonably representative tracer of the high-ionisation compact central region of the system (with very similar morphologies revealed by both Balmer recombination lines and by [O III] λ 4363, all of which are shown in Appendix A). In contrast, the [O II] λ 3726, 3729 emission is both clumpier and spatially more extended, essentially probing the low ionisation gas in the system. Since we observe that $\log(\text{Ne3O2}) > 0$ even in the outskirts, the most plausible explanation is a classical, ‘inside-out’ stratification of the system, although we cannot completely rule out more exotic scenarios such as the presence of diffuse ionised gas (DIG; e.g. Zhang et al. 2017), that typically boosts [O II] λ 3726, 3729 emission (Hunter & Gallagher 1990; Kennicutt 1998) and metal lines strength in general (Garg et al. 2024; McClymont et al. 2024; Clarendon et al. 2025). A recent NIRSpc/IFU study by Hutchison et al. (2025) tentatively claims having identified DIG in a highly-lensed $z \sim 5$ massive post-starburst galaxy. However, while [O II] λ 3726, 3729 emission truly appears enhanced relative to Hydrogen lines in the southern and southwestern regions of our target (compared to the central regions), Hsiao et al. (2025) report non-detections of [N II] λ 6548 and [N II] λ 6583 (these lines are expected to be prominent in regions with DIG) in the MIRI spectra, which challenges the interpretation of DIG being present in the southern-southwestern region of the MACS0647-JD1 system. Of course, at $z > 10$, intrinsically low N/O abundance ratios could also explain the undetected [N II] doublet in the extended region, given that all N/O-enhanced systems tend to be very compact (e.g., Ji et al. 2026).

5.1.2 Shock Modelling: No evidence for shock-driven excitation

Given the tentative position of the spaxels in the south-western region of the system in the AGN dominated region of the Mazzolari et al. (2024) diagnostic diagram, we test the possibility that shocks may have an important contribution to the photoionisation. We use a similar method to D’Eugenio et al. (2025c) who report shock-driven photoionisation in the case of a SFG at $z \sim 4.6$. We use the shock models from the 3MdB database⁴. The grids are computed using the MAPPINGS v code (Sutherland & Dopita 2017). We tested both shock only and shock with precursor models (Allen et al.

2008; Alarie & Morisset 2019) spanning a large parameter space (the *BnZv* space): magnetic field $10^{-4} \mu\text{G} < B < 10 \mu\text{G}$, shock velocity $100 \text{ km s}^{-1} < v < 1000 \text{ km s}^{-1}$, pre-shock (upstream) density $1 \text{ cm}^{-3} < n_{\text{sh}} < 10000 \text{ cm}^{-3}$ and metallicities $10^{-4} < Z < 0.04$. The metallicities are converted to Oxygen abundances values assuming $Z_{\odot} = 0.01524$ and $12 + \log(\text{O}/\text{H})_{\odot} = 8.8$ (assuming the same chemical abundances from Gutkin et al. 2016 as used by the authors in the shock grid calculations and considering a dust depletion $\xi_d = 0.1$, similar to Section 4.5). As before, we choose the $\text{C}/\text{O} = 0.72 (\text{C}/\text{O})_{\odot}$ photoionisation parameters from Gutkin et al. (2016).

In our particular case, we select a fixed magnetic field strength of $B = 10 \mu\text{G}$ for all of the models displayed in Fig. 10. This value is comparable to the magnetic field in the solar neighbourhood ($2 - 25 \mu\text{G}$; Vallee 2022). There is however, plausible evidence the galactic magnetic fields are likely larger in starburst galaxies ($50 - 100 \mu\text{G}$; Beck 2015), and as we go to earlier in the Universe (Wolfe et al. 2008). Because $10 \mu\text{G}$ is the highest value available in the computed shock grids, we regard this value as the most sensible choice. The diagnostic line ratios considered here (O3Hg and Ne3O2) are only weakly sensitive to the magnetic field strength over the range of parameter space probed by our data. In particular, magnetic-field-dependent effects become significant only at very low O3Hg ratios ($\log([\text{O III}] \lambda 4363 / \text{H}\gamma) < -1.5$) where model tracks corresponding to different magnetic fields diverge.

We explore shock model grids with pre-shock densities, $n_{\text{sh}} = 100, 1000$ and 10000 cm^{-3} . Models with $n_{\text{sh}} \lesssim 100 \text{ cm}^{-3}$ are unable to reproduce the observed O3Hg and Ne3O2 measurements in any configuration, so they are strongly disfavoured. For $n_{\text{sh}} = 10^3 - 10^4 \text{ cm}^{-3}$, shock+precursor grids (Fig. 10e and 10f) intersect the data only for parameter combinations that imply oxygen abundances of $12 + \log(\text{O}/\text{H}) \sim 8.2 - 8.4$, exceeding the metallicities inferred from spaxel or clump aperture spectra ($12 + \log(\text{O}/\text{H}) \sim 7.2 - 8.0$ using either the direct or the strong-line method). It is generally true that the metallicities calculated with the direct method could be biased low if shocks are present and not accounted for. This is because shocks alter the ionisation structure of the ISM and can create large temperature variations on small spatial scales. As a result, the electron temperature and the oxygen abundance may be decoupled and the metallicities would be underestimated in the shock-heated regions. However, the shock grid from Fig. 10e further requires high velocity shocks ($\sim 500 - 1000 \text{ km s}^{-1}$) to match our data. Such velocities are substantially higher than the characteristic ionized-gas kinematic widths in our system (FWHM $\sim 100 - 350 \text{ km s}^{-1}$) and our spectral fits show no statistical requirement for an additional broader component, together suggesting that these shock plus pre-cursor models are disfavoured. A shock-only model with $B = 10 \mu\text{G}$ and $n_{\text{sh}} = 10^4 \text{ cm}^{-3}$ (Fig. 10c) can reproduce the observed line ratios in the case of the SE and NW clump apertures at lower metallicities and lower shock velocities than the shock plus pre-cursor cases. However, an upstream density of 10^4 cm^{-3} is already one order of magnitude above the electron density of $\log(n_e/\text{cm}^{-3}) = 3.3^{+0.7}_{-0.6}$, derived from the full-aperture spectrum of MACS0647-JD1 image (Abdurro’uf et al. 2024). Moreover, shocks compress the gas by at least a factor of four in the strong adiabatic shock limit (and potentially more if radiative), implying post-shock densities $\geq 4 \times 10^4 \text{ cm}^{-3}$. We therefore conclude that shock excitation is unlikely to be the primary origin of the observed line ratios.

5.1.3 Spatially resolved properties of the ISM gas

Based on our methods for calculating the strong-line metallicity (discussed in Section 4.5), we obtain the map shown in Fig. 9. We did a similar spatial cut of the map in order to facilitate the compar-

⁴ <https://sites.google.com/site/mexicanmillionmodels/>

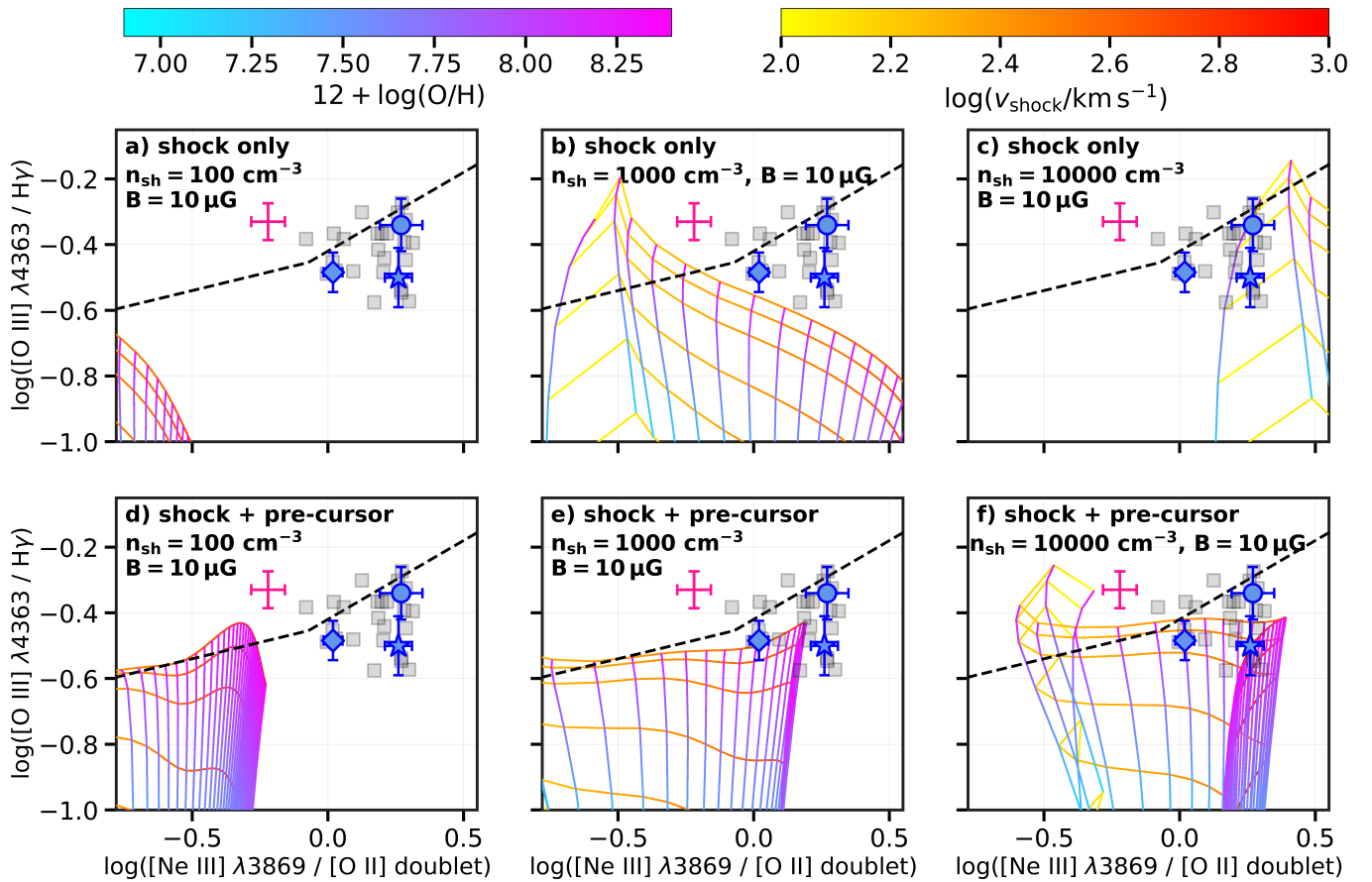


Figure 10. In this figure, we illustrate the various shock models that we overlaid on the [Mazzolari et al. \(2024\)](#) diagnostic diagram, in order to compare with our data-points. Individual spaxels are marked with grey squares (with the pink error bars showing their median uncertainties), whereas the blue symbols have similar meanings to [Fig. 6a](#): the diamond represent the full-aperture, the star is the SE clump and the circle is the NW clump. The black, dashed line is the demarcation between the AGN-dominated regime and the regions where SF and AGN have similar contributions to photoionisation (SF or AGN regime). We display a number of shock and shock + pre-cursor grids computed using MAPPINGS v ([Sutherland & Dopita 2017](#)) at fixed pre-shock density, n_{sh} , fixed magnetic field, $B = 10 \mu\text{G}$ and varying metallicity $7 < 12 + \log(\text{O}/\text{H}) < 8.4$ and shock velocity $2 < \log(v_{\text{shock}} / \text{km s}^{-1}) < 3$. Our observations can only be reproduced with either high metallicities or high pre-shock densities, which, although not completely ruled out locally, are difficult to reconcile with the gas-phase metallicities ([Fig. 5c](#)) and electron densities inferred by [Abdurro'uf et al. \(2024\)](#) for our system.

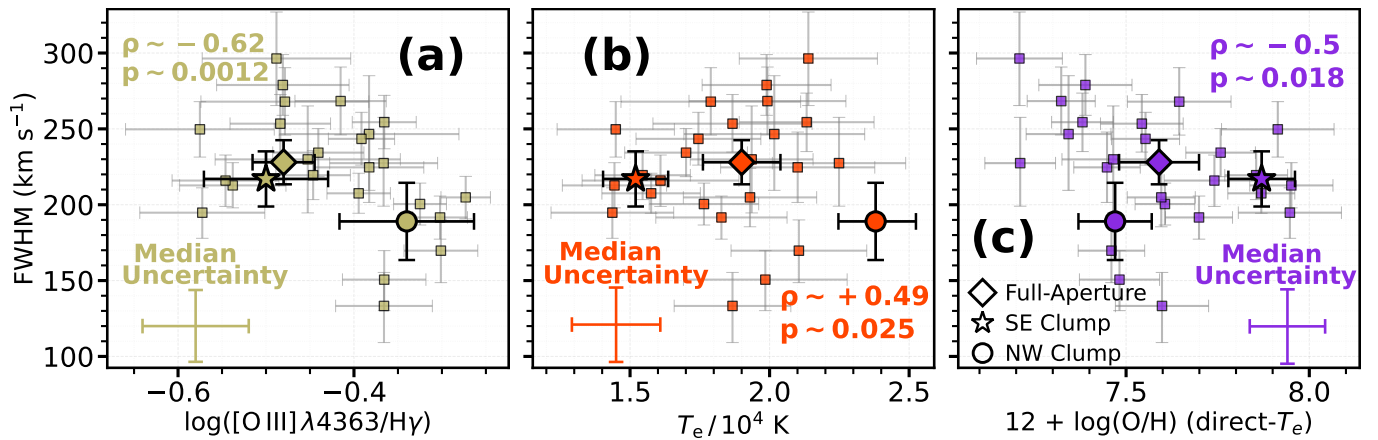


Figure 11. This figure shows the variation of gas velocity dispersion (FWHM) as a function of O3Hg line ratio ([Fig. 11a](#)), electron temperature ([Fig. 11b](#)) or gas-phase metallicity calculated using the direct method ([Fig. 11c](#)). As before, we only show the spaxels with $S/N_{[\text{O III}]\lambda 4363} > 3$, but we also show the values corresponding to the SE and NW clump and for the full-aperture spectra. We display the individual and the typical median uncertainties for the per-spaxel measurements. The bootstrapped median Spearman correlation coefficient ρ and the p-value are reported for the set of correlations considered.

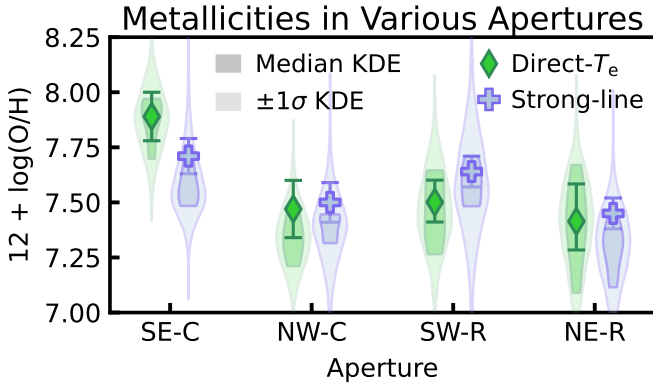


Figure 12. This figure shows the calculated gas-phase metallicities (using both the direct- T_e and the strong-line methods) and the uncertainties for the spectra of the four apertures identified in Fig. 2b. For each aperture and method, violin plots illustrate the metallicities of spaxels within the said aperture. Darker-shade violins show the kernel density estimate (KDE) of median metallicities, while lighter-shaded violins include $\pm 1\sigma$ spaxel-level uncertainties.

ison with the direct metallicity map (Fig. 5c). We notice that our results are consistent between these methods. Both the direct- T_e and the strong-line methods reveal that the SE clump is more enriched compared to both the NW clump and the turbulent, metal-poor gas located in the NE region of the system (i.e. between the two clumps).

To provide quantitative evidence of the different nature of the ISM at various locations, we divide our observed system within the field-of-view in four different regions, as shown in Fig. 2: the north-west and the south-east clumps (SE-C and NW-C), together with the north-east and south-west regions (NE-R and SW-R). We illustrate the resulting direct- T_e and strong-line metallicities from the integrated spectra of these four apertures (obtained by adding up the spaxels within each of them) in Fig. 12. We find that, for each aperture, the two methods of calculating the metallicity give consistent results. Moreover, Fig. 12 shows that, although some non-negligible spaxel-to-spaxel variations may occur in our maps, our conclusion that the SE clump is more metal-rich than its surrounding environment is statistically sound.

Fig. 5a, 5c, and 5d reveal spatial variations in gas kinematics, excitation, and chemical properties across the system, suggesting possible connections between gas velocity dispersion, excitation-sensitive line ratios (O3Hg in particular), and gas-phase metallicity on spatially resolved scales. We quantify these trends by testing for spaxel-scale correlations between gas velocity dispersion (FWHM) and properties of the ISM. We find a significant anti-correlation between FWHM and the O3Hg line ratio (with a p-value of 1.2×10^{-3} and a Spearman correlation coefficient $\rho \sim -0.62$; Fig. 11a). In contrast, we found only a marginal anti-correlation between either FWHM and metallicity, and a tentative positive correlation of FWHM and electron temperature (as shown in Fig. 11b and Fig. 11c). Our analysis does not find any correlation between FWHM and Ne3O2 ($p \sim 0.22$), although central spaxels tend to have both high O3Hg and Ne3O2 ratios. We caution that the reported Spearman coefficients and p-values are based on median estimates using face-value measurements in spaxels with $S/N > 3$ in [O III] $\lambda 4363$. A bootstrap analysis accounting for per-spaxel uncertainties yields p-values exceeding 0.05 for the FWHM- T_e and FWHM-metallicity relations, indicating that these trends are not robust. Only the correlation between FWHM and O3Hg remains significant, with an 84th-percentile p-value of 0.028.

The differing strengths of these correlations likely reflect the fact

that O3Hg is a direct and un-biased observable, but which is sensitive to both the local excitation and thermal conditions of the ionized gas in the ISM, and also to the local instantaneous SFR. On the other hand, the electron temperature and the inferred metallicity are derived quantities subject to additional assumptions and associated systematic uncertainties. The most important of these are a secondary dependence on the ionisation parameter, the possibility of multi-zone ISM (see e.g., Marconi et al. 2024), as well as possible uncertain dust corrections in calculations of metallicities and electron temperatures. Importantly, a locally elevated temperature of the O^{++} gas may not necessarily imply a higher [O III] $\lambda 4363 / H\gamma$ ratio. While the effective $H\gamma$ recombination rate has a weak inverse dependence on electron temperature, this effect can be easily outweighed by spatial variations in electron and ion densities or gas filling factor, particularly in a complex, multi-zone ISM. The gas FWHM traces gas emission lines broadening due to both thermal and non-thermal processes. Physically, the presence of dynamically turbulent and hot gas (as shown in Fig. 5d and 7b) between the two clumps may indicate enhanced energy injection into the ISM which, given that we have shown a shock-driven photoionisation scenario to be disfavoured by our observations (Section 5.1.2), could instead arise from a combination of star formation-driven feedback and complex gravitational interactions between the two main clumps and the surrounding metal-poor gas in the NW and SE regions of the system.

Our results disagree with results from the local Universe and lower redshift studies, which find positive correlations between gas-phase metallicity and (stellar) velocity dispersion for massive, evolved galaxies (e.g., Li et al. 2018; Cappellari 2023). Such a positive correlation is also seen in individual galaxies within the SPT0311-58 protocluster at $z \sim 6.9$ (Arribas et al. 2024). The possible anti-correlation observed in the case of MACS0647-JD is likely not the result of secular interplaying processes shaping the co-evolution of various galaxy properties. Such processes have not been established yet in low-mass systems at $z > 10$. Instead, our findings suggest that our target is observed in an early short-lived evolutionary phase.

5.1.4 Spatially resolved stellar populations: bursty star formation in the north-eastern region of the system

We compute the burstiness of star formation on a spaxel-by-spaxel scales using the SFR averaged over the last 100 Myr in look-back time (SFR_{100} from our PROSPECTOR SED fits) to probe the long timescale SFR. For instantaneous/short timescale SFR, we use two alternative tracers: a) SFR_{10} (similar to SFR_{100} but it probes only the last 10 Myr in look-back time; this is also computed by PROSPECTOR) and b) $SFR_{H\gamma}$ inferred based on the $H\gamma$ line integrated flux. In order to estimate $SFR_{H\gamma}$, we first correct the $H\gamma$ fluxes of each spaxel based on the observed $H\beta/H\gamma$ Balmer decrement corresponding to the said spaxel (and we assume no dust correction in the cases where the $H\beta/H\gamma$ ratio from the spectrum is lower than the case-B value of 2.105). We then assume an intrinsic, case-B $H\alpha/H\gamma = 5.79$ ratio, valid for an electron temperature $T_e \sim 20000$ K (Groves et al. 2012) and we adapt the $H\alpha$ -SFR Kennicutt relation from equation (12) of Kennicutt & Evans (2012) as follows:

$$\log SFR_{H\gamma} \left(M_{\odot} \text{ yr}^{-1} \right) = \log L_{H\gamma} \left(\text{erg s}^{-1} \right) - 40.5 - \log \mu - 0.3. \quad (5)$$

Here, for de-lensing, we assume the lensing magnification of the system is $\mu = 8 \pm 1$ (Chan et al. 2017). However, the SFR- $H\alpha$ equation derived by Kennicutt & Evans (2012) is calibrated in the local Universe, assuming a solar metallicity and a Calzetti et al. (2000) dust attenuation law, but at higher redshifts, galaxies typically have

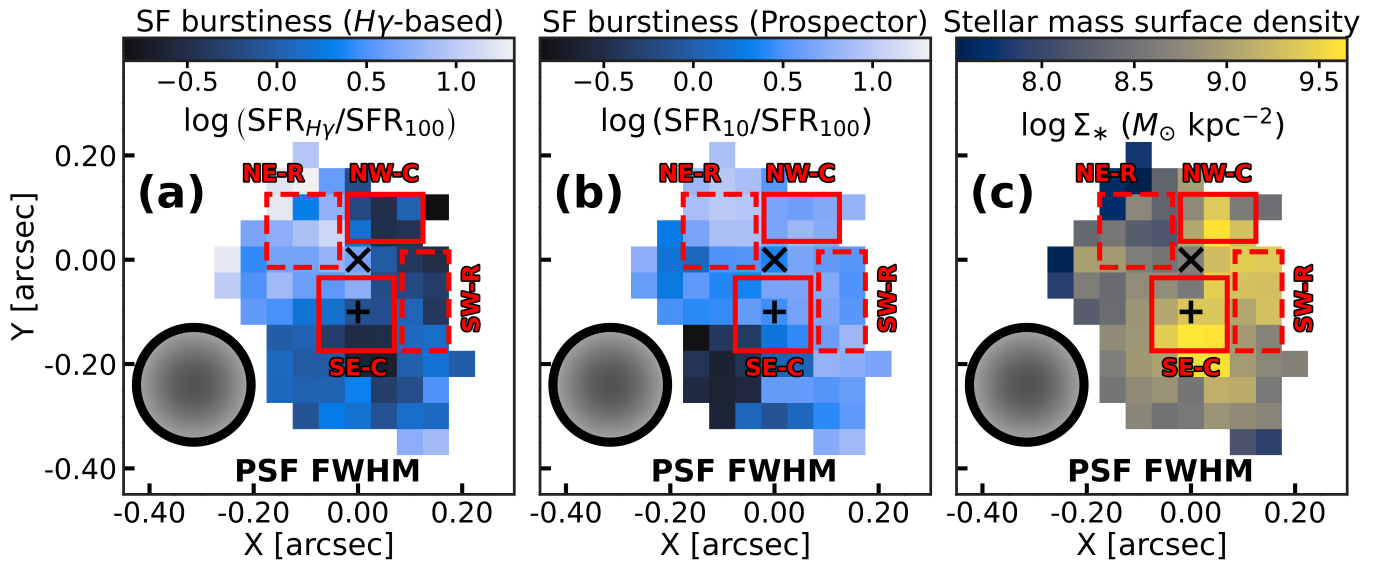


Figure 13. In this figure, we display the spatially resolved star formation burstiness in MACS0647-JD1 system. The burstiness probes the recent versus prolonged star formation activity in our target, and is defined in two alternative ways: $\text{SFR}_{\text{Hy}}/\text{SFR}_{100}$ (Fig. 13a) and $\text{SFR}_{10}/\text{SFR}_{100}$ (Fig. 13b). The magenta rectangles are the apertures corresponding to the two clumps (SE and NW, as identified from NIRCcam F444W imaging; see Fig. 2). Both these maps consistently show a remarkable recent star formation enhancement in the north-east region and a less bursty SFH, particularly in the region of the more massive SE clump. Fig. 13c shows the stellar mass density map of this system and confirms the more massive nature of the two clumps, compared to other regions. On all panels, we only show the spaxels with a $S/N > 5$ detection of $\text{H}\gamma$ from our analysis of NIRSpc/IFU data. We also show the PSF size in all panels, together with the centroid of stellar continuum (+ cross) and of the $\text{H}\gamma$ emission line map (x cross).

different properties to the local targets, so a more suitable set of assumptions is a different dust attenuation law and a lower metallicity. Reddy et al. (2022) and Shapley et al. (2023) showed that the correction term is around -0.3 dex if we instead assume a Small Magellanic Cloud dust attenuation law and a metallicity of $0.27 Z_{\odot}$.

We show our results in Fig. 13a and Fig. 13b. Both panels agree on finding a significant recent star formation enhancement in the NE region, the same location where the gas is both more turbulent (Fig. 5d) and metal-poor (Fig. 5c). On the other hand, the more massive, more metal-enriched SE clump does not undergo a noticeable starburst episode within the timescales probed. As shown in Fig. 13b, we find only a moderate burstiness in the case of the two clumps (more pronounced for the NW clump). Fig. 13c confirms the more massive nature of the two clumps compared to the surrounding regions. The stellar mass densities of the spaxels in the NE region are typically ~ 1 dex below the values within the two clumps, which implies that this region may be associated with a metal poor gas inflow; another plausible scenario could be that this region contains gas stripped from the NW clump by gravitational interactions with the massive SE clump. Indeed, the metallicities of the NE-R and NW-C are consistent within the uncertainties as shown in Fig. 12.

More puzzlingly, the SW region of the system (which is intrinsically fainter than either of the clumps in both NIRCcam F444W and NIRSpc/IFU) appears to be substantially more massive than the bursty, low- M_* NE region; in addition, SFR_{Hy} finds a negligible star formation (SF) enhancement (Fig. 13a), and when the recent SF is probed via SFR_{10} , a starburst effect is observed in the SW region, but it is still less intense than in the NE region. Physically, the SW region could represent gas and stars that originated in the SE clump, but which get re-distributed during a merger event.

5.1.5 Merging galaxies or clumps in a disc?

The observed properties of MACS0647-JD1 allow, in principle, two broad interpretations: either the system represents a gas-rich rotating disc hosting multiple clumps, or it is caught during an early-stage merger between two distinct components. Disc galaxies are generally characterised by a ratio of ionised gas velocity to velocity dispersion of $V_{\text{gas}}/\sigma \gtrsim 1$ and, additionally, by ordered rotation on spatially resolved scales (Förster Schreiber & Wuyts 2020; Danhaive et al. 2025c). In Appendix C, we show that the observed rotational pattern in the velocity field of the MACS0647-JD1 system may be dominated by instrument systematics and it is difficult to retrieve the intrinsic velocity field. However, one reason why we cannot firmly dismiss the hypothesis of a real rotating structure is the fact that the rotational gradient is spatially more extended than the FWHM of the PSF (the latter being ~ 4.4 spatial pixels). In addition, as we argue in Appendix C, the amplitude of the artificial rotation pattern produced due to the slit-width effect (described in Isobe et al. 2023a and Appendix C) is noticeably smaller (2.6 times) than the observed velocity gradient in our data. It is, however, crucial to note that we only provide a simplified calculation that illustrates that the slit-width effect could possibly mimic rotational pattern in *JWST/NIRSpc* IFU data. Distinguishing instrumental effects from genuine galaxy kinematics would definitely require additional IFU observations obtained at a position angle rotated by 90° relative to the current setup (Fig. C2a).

In this section, we argue that the morphological, chemical and kinematical properties of this system are more naturally explained by a scenario involving a gas-rich merger between the NW and the SE clumps. First and foremost, the two main components exhibit markedly different gas-phase metallicities (see Section 5.1.3), with the SE clump being significantly more enriched than both the north-west clump and the surrounding gas. Using the values in Table 1, we obtain a metallicity difference of 0.42 ± 0.18 dex (using direct-method metallicities; or 0.22 ± 0.12 dex using the metallicities derived based

on the strong-line method) between the two main components of the system. Such metallicity contrasts on short projected physical scales (~ 300 pc in the source frame, assuming a magnification of $\mu \sim 8$) are difficult to reconcile with in-situ clump formation within a single disc, where clumps primarily form out of the existing ISM gas reservoir. While several works revealed metallicity inhomogeneities in proto-disc systems at $z > 6$ (Arribas et al. 2024; Venturi et al. 2024; Ivey et al. 2026), the reported metallicity gradients are $|\nabla_r \log(\text{O}/\text{H})| \lesssim 0.2 \text{ dex kpc}^{-1}$. The amplitude of the variations we measure in the MACS0647-JD system suggests that additional processes beyond simple in-situ fragmentation (such as external fresh gas accretion or mergers) may be involved.

Second, the highest gas velocity dispersions are observed in the regions outside the two massive clumps (Fig. 5d) and are anti-correlated with excitation-sensitive line ratios (Fig. 11a). This suggests that turbulence is not primarily driven by star formation feedback, as expected in clumpy discs, but by gravitational interactions possibly leading to a large-scale circulation of the gas, consistent with a merger scenario. The observation of this dynamically hot gas in the regions outside the main components is facilitated by the lack of strong stellar sources in these locations, allowing the emission lines to probe large path lengths along the line of sight and therefore trace wide-scale motions of the gas. In addition, the star formation burstiness maps show a clear asymmetry (Fig. 13): the most intense enhancement of recent star formation is in the north-east region, co-spatial with confidently identified metal-poor, high turbulence gas.

Third, the centroid of nebular emission is significantly offset from the stellar continuum peak by at least two spatial pixels ($\sim 0.1''$) as measured using the H γ emission map; see Fig. 2, but the spatial offset is larger if we consider, for instance, H β , H δ or [Ne III] $\lambda 3869$ centroids. While instrument systematics were shown to sometimes create an artificial shift of the centroid of point sources as a function of wavelength, the magnitude of this effect is too small ($\sim 0.02''$; Beck 2025) to justify the different spatial distribution of stellar continuum and line emission light. In a clumpy disc, the most intense line emission is generally co-spatial with the dominant stellar clumps, whereas star formation between stellar components is more naturally explained by merger-driven gas instability.

Although an accurate estimate of the gas mass in the system would require the completion of the existing allocated *NOEMA* observations, we could provide a crude estimate using a method similar to Nakajima et al. (2025). Given our de-lensed value of the SFR $_{\text{H}\gamma}$ estimated for the full-aperture of $5.5 \pm 1.0 M_{\odot} \text{ yr}^{-1}$ (Table 1) and an effective radius of 70 ± 24 pc (Hsiao et al. 2024a), we obtained a SFR density of $\log(\Sigma_{\text{SFR}_{\text{H}\gamma}}/M_{\odot} \text{ yr}^{-1} \text{ kpc}^{-2}) = 2.25 \pm 0.30$. We use equation (2) from Bouché et al. (2007) to estimate the gas mass surface density. In this equation from Bouché et al. (2007), $\Sigma_{\text{SFR}} \propto \Sigma_{\text{gas}}^{1.71 \pm 0.05}$ and the power-law index of 1.71 ± 0.05 is significantly larger than the 1.4 ± 0.15 value given in Kennicutt (1998). This substantial difference arises because of collisionally enhanced star formation efficiency in high density gas ($\sim 1000 \text{ cm}^{-3}$), a regime which is more commonly observed in the ISM of high-redshift galaxies. With our previous value of $\log \Sigma_{\text{SFR}_{\text{H}\gamma}}$, we obtain $\log(\Sigma_{\text{gas}}/M_{\odot} \text{ pc}^{-2}) = 3.70 \pm 0.32$ implying $\log(M_{\text{gas}}/M_{\odot}) = 8.20 \pm 0.34$. This indicates that the gas mass in the MACS0647-JD1 is at least comparable, but most likely larger than the stellar mass within the two SE and NW clumps.

In the hypothesis that the system is a rotating disc, we can obtain an estimate for its dynamical mass, using the following equation (adapted from Cappellari et al. 2006):

$$M_{\text{dyn}} \approx \frac{5R_{\text{eff}} \sigma_*^2}{G}. \quad (6)$$

We assume an effective radius $R_{\text{eff}} = 70 \pm 24$ pc (Hsiao et al. 2024a) and we estimate the stellar velocity dispersion based on the gas velocity dispersion, $\sigma_{\text{gas}} = \text{FWHM}_{\text{gas}}/2.355 = 97 \pm 8 \text{ km s}^{-1}$ (for the full-aperture spectrum) and assuming the empirical relation: $\sigma_* \approx 1.26 \times \sigma_{\text{gas}} \approx 122 \pm 10 \text{ km s}^{-1}$ (Bezanson et al. 2018). We obtain $\log(M_{\text{dyn}}/M_{\odot}) = 9.1 \pm 0.5$. The quoted uncertainty takes into account the systematics of the virial mass estimator equation and the systematics associated with choosing a factor of 5 in Equation 6, instead of using equation (7) from van der Wel et al. (2022), which accounts more accurately for variations due to object's axial ratio and Sérsic index. However, given the two-clump morphology of our target (Fig. 2b), a simple single Sérsic profile fit to the F444W image of MACS0647-JD1 would be unphysical.

The dynamical mass of the system is statistically larger than the combined mass of the stars (see Table 1) and gas. Dark matter, on the other hand, is even more difficult to accurately constrain at such high redshifts. However, galaxies at $z > 4$ and $\log(M_*/M_{\odot}) < 9$ are expected to be strongly dark matter dominated, as revealed by recent *JWST* spectroscopic observations (de Graaff et al. 2024a; Danhaive et al. 2025b) and simulations (de Graaff et al. 2024b; McClymont et al. 2026). Fig. 13c illustrates a clear double-peaked stellar-mass density distribution, with two spatially distinct mass concentrations corresponding to the south-eastern and north-western stellar components. In order for a disc-like galaxy to maintain long-term gravitational stability, however, the total mass (including stars, gas and dark matter) profile should be peaked at the centre. We cannot use the stellar mass map morphology (Fig. 13c) to argue against a dynamically stable disc, because such an argument would require a detailed analysis of the spatial distribution of gas and dark matter mass in this system.

6 SUMMARY AND CONCLUSIONS

In this paper, we present a spatially resolved analysis of the ISM in MACS0647-JD1, the brightest galaxy currently known at $z > 10$ (owing to gravitational lensing), using medium-resolution NIRSpect/IFU G395M observations from the GA-NIFS GTO programme. We present a novel method of extrapolating the *JWST* spectra outside the nominal wavelength range of the G395M grating and thus obtain the H β -wavelength collapsed flux map for a target at $z \sim 10.2$. By combining these spectroscopic data with archival *JWST* imaging, we infer star-formation histories across different regions of the system, enabling a detailed investigation of the physical processes governing its early assembly. This approach provides new insight into the complex interplay between star formation activity and chemical enrichment in one of the earliest starburst systems known. We summarise our conclusions as follows:

- The system consists of two bright components detected in NIRSpect/IFU and NIRCам imaging. The stellar continuum centroid coincides with the more massive component, which is spatially offset compared to the emission-line centroid by 150 pc (in the source plane). This is most likely a sign-post of recent star formation activity in between the two components, potentially triggered as a result of a pre-coalescence merger event.
- Our target provides the highest-redshift measurement of direct metallicity obtained by NIRSpect, and the second highest- z measurement with any instrument, surpassed only by GNz11 (Bunker et al.

2023; Álvarez-Márquez et al. 2025). We compute metallicities from spaxel spectra using two independent approaches: the direct method (based on the electron temperature) and a customised strong-line calibration. Both methods yield consistent results within the uncertainties. We find that the brighter south-eastern clump is more metal-rich ($12 + \log(\text{O}/\text{H})_{\text{direct}} = 7.89 \pm 0.11$), while the north-western clump is less enriched ($12 + \log(\text{O}/\text{H})_{\text{direct}} = 7.47 \pm 0.14$). Such a pronounced asymmetry would be difficult to explain if the two components were clumps within a single rotating disc. Although we attempted to reconstruct the velocity field (see Appendix C), the current data do not provide conclusive evidence for an ordered rotation pattern.

- The strong-line metallicities are less reliable in the south-western part, where the unusual morphology of the $[\text{O II}] \lambda\lambda 3726, 3729$ emission (as compared to high-ionisation or Hydrogen recombination lines), together with tentative AGN-like signatures on one of the Mazzolari et al. (2024) diagnostic diagrams, could possibly imply the presence of diffuse ionised gas or a complex stratification structure. We have additionally shown that shocks are strongly disfavoured, although not completely ruled out by our observed emission line ratios.

- We analyse the ISM conditions on spatially resolved scales, by focusing on various diagnostic ratios. Analysing the individual spaxel spectra, we find a meaningful anti-correlation between the gas velocity dispersion (FWHM; a tracer of turbulence) and $[\text{O III}] \lambda 4363/H\gamma$ line ratio (a proxy for the excitation state of the ISM), but statistically weaker trends between FWHM and gas-phase metallicity or electron temperature, both of which are likely influenced by a secondary dependence on the ionisation parameter.

- Combining our spectroscopic and stellar populations analyses, we demonstrated that, remarkably, the north-eastern region has a small stellar mass and predominantly contains metal-poor gas, but the star formation burstiness is significantly elevated compared to the surroundings. This suggests that a very recent star formation event has been initiated in that region, which could be either associated with a fresh gas inflow or a re-distribution of the metal-poor gas already existing in the north-western component, as a result of gravitational interaction. These two scenarios could possibly explain the metallicity difference between the south-eastern and north-western components, which are massive gas clumps, with only little to moderate burstiness.

ACKNOWLEDGEMENTS

We thank Dr Xihan Ji for insightful comments that led to a better interpretation of our PROSPECTOR fitting and results. RGP acknowledges funding support from a STFC PhD studentship. RGP, FDE, RM, GCJ, JS and LRI acknowledge support by the Science and Technology Facilities Council (STFC), by the ERC through Advanced Grant 695671 “QUENCH”, and by the UKRI Frontier Research grant RISEandFALL. RM also acknowledges funding from a research professorship from the Royal Society. QD acknowledges a PhD studentship from Trinity College, Cambridge. YI is supported by JSPS KAKENHI Grant No. 24KJ0202 and 24KJ1160. HÜ acknowledges funding by the European Union (ERC APEX 101164796). Views and opinions expressed are however those of the authors only and do not necessarily reflect those of the European Union or the European Research Council Executive Agency. Neither the European Union nor the granting authority can be held responsible for them. SZ, SC and GV acknowledge support from the European Union’s HE ERC Starting Grant No. 101040227 - WINGS. IL acknowledges support from PRIN-MUR project “PROMETEUS” financed by the

European Union - Next Generation EU, Mission 4 Component 1 CUP B53D23004750006. AJB and GCJ acknowledge funding from the “FirstGalaxies” Advanced Grant from the European Research Council (ERC) under the European Union’s Horizon 2020 research and innovation program (Grant Agreement No. 789056). BRP, SA and MP acknowledge grant PID2021-127718NB-I00 funded by the Spanish Ministry of Science and Innovation/State Agency of Research (MICIN/AEI/ 10.13039/501100011033); MP also acknowledges the grants RYC2023-044853-I and PID2024-159902NA-I00, funded by MICIU/AEI/10.13039/501100011033 and European Social Fund Plus (FSE+). BRP also acknowledges support by the grant PID2024-158856NA-I00. MC acknowledges support from ESO via the ESO Fellowship Europe. EB and GC acknowledge the INAF GO grant “A JWST/MIRI MIRACLE: Mid-IR Activity of Circumnuclear Line Emission” and the “Ricerca Fondamentale 2024” INAF program (mini-grant 1.05.24.07.01). TH was supported by JSPS KAKENHI 25K00020. ST acknowledges support from the Royal Society Research Grant G125142. JW acknowledges support from the Cosmic Dawn Center through the DAWN Fellowship; the Cosmic Dawn Center (DAWN) is funded by the Danish National Research Foundation under grant No. 140.

DATA AVAILABILITY

This work is based on observations with the NASA/ESA/CSA James Webb Space Telescope. The data were obtained as part of the JWST program ID 4528 (Cycle 3, PI: K. Isaak). These data are available from [Mikulski Archive for Space Telescopes](#) at the Space Telescope Science Institute, which is operated by the Association of Universities for Research in Astronomy, Inc., under NASA contract NAS 5-03127 for JWST. The reduced datacube is available upon reasonable request. The photometry data are available from the public DAWN JWST Archive (DJA) data ⁵.

REFERENCES

- Abdurro’uf et al., 2024, *ApJ*, 973, 47
 Agertz O., et al., 2020, *MNRAS*, 491, 1656
 Alarie A., Morisset C., 2019, *Rev. Mex. Astron. Astrofis.*, 55, 377
 Allen M. G., Groves B. A., Dopita M. A., Sutherland R. S., Kewley L. J., 2008, *ApJS*, 178, 20
 Álvarez-Márquez J., et al., 2025, *A&A*, 695, A250
 Arellano-Córdova K. Z., et al., 2022, *ApJ*, 940, L23
 Arribas S., et al., 2024, *A&A*, 688, A146
 Astropy Collaboration et al., 2022, *ApJ*, 935, 167
 Bacon R., et al., 1995, *A&AS*, 113, 347
 Baker W. M., et al., 2023, *MNRAS*, 519, 1149
 Baker W. M., et al., 2025, *A&A*, 697, A90
 Beck R., 2015, *A&ARv*, 24, 4
 Beck T., 2025, Technical Report Technical Report JWST-STScI-009029, Evidence for Problems in the JWST NIRSpec IFU Calibration Distortion Model. STScI
 Bezanson R., et al., 2018, *ApJ*, 868, L36
 Böker T., et al., 2022, *A&A*, 661, A82
 Bouché N., et al., 2007, *ApJ*, 671, 303
 Bourne M. A., Yang H.-Y. K., 2023, *Galaxies*, 11, 73
 Boyett K., et al., 2024, *MNRAS*, 535, 1796
 Bradley L., et al., 2024, *astropy/photutils*: 2.0.2, doi:10.5281/zenodo.596036
 Brammer G., 2023, *grizli*, doi:10.5281/zenodo.8370018

⁵ Available at <https://s3.amazonaws.com/grizli-v2/jwstMosaics/v7/index.html>

- Bunker A. J., et al., 2023, *A&A*, 677, A88
- Bunker A. J., et al., 2024, *A&A*, 690, A288
- Byler N., Dalcanton J. J., Conroy C., Johnson B. D., 2017, *ApJ*, 840, 44
- Calabrò A., et al., 2024, *ApJ*, 975, 245
- Calzetti D., Armus L., Bohlin R. C., Kinney A. L., Koornneef J., Storchi-Bergmann T., 2000, *ApJ*, 533, 682
- Cameron A. J., et al., 2023, *A&A*, 677, A115
- Cappellari M., 2017, *MNRAS*, 466, 798
- Cappellari M., 2023, *MNRAS*, 526, 3273
- Cappellari M., et al., 2006, *MNRAS*, 366, 1126
- Carniani S., et al., 2024, *Nature*, 633, 318
- Castellano M., et al., 2024, *ApJ*, 972, 143
- Cataldi E., et al., 2025, *A&A*, 703, A208
- Chabrier G., 2003, *PASP*, 115, 763
- Chan B. M. Y., Broadhurst T., Lim J., Diego J. M., Zitrin A., Coe D., Ford H. C., 2017, *ApJ*, 835, 44
- Charlot S., Fall S. M., 2000, *ApJ*, 539, 718
- Choi J., Dotter A., Conroy C., Cantiello M., Paxton B., Johnson B. D., 2016, *ApJ*, 823, 102
- Choustikov N., et al., 2025, *arXiv e-prints*, p. arXiv:2510.06347
- Christensens L., et al., 2012, *MNRAS*, 427, 1953
- Claeysens A., Adamo A., Richard J., Mahler G., Messa M., Dessauges-Zavadsky M., 2023, *MNRAS*, 520, 2180
- Clarendon A., Strom A., von Raesfeld C., 2025, *Research Notes of the American Astronomical Society*, 9, 206
- Coe D., et al., 2013, *ApJ*, 762, 32
- Conroy C., Gunn J. E., 2010, *ApJ*, 712, 833
- Conroy C., et al., 2009, *ApJ*, 699, 486
- Costantin L., et al., 2023, *ApJ*, 946, 71
- Covelo-Paz A., et al., 2026, *A&A*, 705, A155
- Curti M., et al., 2023, *MNRAS*, 518, 425
- Curti M., et al., 2024, *A&A*, 684, A75
- Curti M., et al., 2025, *A&A*, 697, A89
- Curtis-Lake E., et al., 2023, *Nature Astronomy*, 7, 622
- D'Eugenio F., et al., 2024a, *Nature Astronomy*, 8, 1443
- D'Eugenio F., et al., 2024b, *A&A*, 689, A152
- D'Eugenio F., et al., 2025a, *arXiv e-prints*, p. arXiv:2503.11752
- D'Eugenio F., et al., 2025b, *ApJS*, 277, 4
- D'Eugenio F., et al., 2025c, *MNRAS*, 536, 51
- D'Eugenio F., et al., 2025d, *MNRAS*, 542, 960
- Danhaive A. L., et al., 2025a, *arXiv e-prints*, p. arXiv:2510.06315
- Danhaive A. L., et al., 2025b, *arXiv e-prints*, p. arXiv:2510.14779
- Danhaive A. L., et al., 2025c, *MNRAS*, 543, 3249
- Davé R., Finlator K., Oppenheimer B. D., 2011, *MNRAS*, 416, 1354
- De Lucia G., Xie L., Fontanot F., Hirschmann M., 2020, *MNRAS*, 498, 3215
- De Rossi M. E., Bower R. G., Font A. S., Schaye J., Theuns T., 2017, *MNRAS*, 472, 3354
- Dekel A., et al., 2009, *Nature*, 457, 451
- Díaz A. I., Castellanos M., Terlevich E., Luisa García-Vargas M., 2000, *MNRAS*, 318, 462
- Dome T., Tacchella S., Fialkov A., Ceverino D., Dekel A., Ginzburg O., Lapiner S., Looser T. J., 2024, *MNRAS*, 527, 2139
- Donnan C. T., et al., 2025, *arXiv e-prints*, p. arXiv:2507.10518
- Dorner B., et al., 2016, *A&A*, 592, A113
- Dors O. L., Maiolino R., Cardaci M. V., Hägele G. F., Krabbe A. C., Pérez-Montero E., Armah M., 2020, *MNRAS*, 496, 3209
- Dressler A., et al., 2024, *ApJ*, 964, 150
- Duan Q., et al., 2024, *arXiv e-prints*, p. arXiv:2411.04944
- Duan Q., et al., 2025, *MNRAS*, 540, 774
- Ebeling H., Barrett E., Donovan D., Ma C. J., Edge A. C., van Speybroeck L., 2007, *ApJ*, 661, L33
- Endsley R., Chisholm J., Stark D. P., Topping M. W., Whittler L., 2025, *ApJ*, 987, 189
- Fabian A. C., 2012, *ARA&A*, 50, 455
- Falcón-Barroso J., et al., 2011, *A&A*, 532, A95
- Faucher-Giguère C.-A., 2018, *MNRAS*, 473, 3717
- Ferland G. J., et al., 2013, *Rev. Mex. Astron. Astrofis.*, 49, 137
- Ferland G. J., et al., 2017, *Rev. Mex. Astron. Astrofis.*, 53, 385
- Ferrara A., Pallottini A., Sommovigo L., 2025, *A&A*, 694, A286
- Ford H. C., et al., 2003, in *Future EUV/UV and Visible Space Astrophysics Missions and Instrumentation*, pp 81–94, doi:10.1117/12.460040
- Foreman-Mackey D., Hogg D. W., Lang D., Goodman J., 2013, *PASP*, 125, 306
- Förster Schreiber N. M., Wuyts S., 2020, *ARA&A*, 58, 661
- Fujimoto S., et al., 2023, *ApJ*, 949, L25
- Fujimoto S., et al., 2024, *ApJ*, 977, 250
- Fujimoto S., et al., 2025a, *arXiv e-prints*, p. arXiv:2510.16116
- Fujimoto S., et al., 2025b, *Nature Astronomy*, 9, 1553
- García A. M., et al., 2024, *MNRAS*, 531, 1398
- García A. M., et al., 2025, *arXiv e-prints*, p. arXiv:2510.26877
- Gardner J. P., et al., 2023, *PASP*, 135, 068001
- Garg P., Narayanan D., Sanders R. L., Davé R., Popping G., Shapley A. E., Stark D. P., Trump J. R., 2024, *ApJ*, 972, 113
- Geris S., et al., 2026, *MNRAS*, 545, staf1979
- Gibson B. K., Pilkington K., Brook C. B., Stinson G. S., Bailin J., 2013, *A&A*, 554, A47
- Greene J. E., et al., 2024, *ApJ*, 964, 39
- Groves B., Brinchmann J., Walcher C. J., 2012, *MNRAS*, 419, 1402
- Gutkin J., Charlot S., Bruzual G., 2016, *MNRAS*, 462, 1757
- Hainline K. N., et al., 2024, *ApJ*, 964, 71
- Harikane Y., Nakajima K., Ouchi M., Umeda H., Isobe Y., Ono Y., Xu Y., Zhang Y., 2024, *ApJ*, 960, 56
- Hayes M. J., Saldana-Lopez A., Citro A., James B. L., Mingozi M., Scarlata C., Martinez Z., Berg D. A., 2025, *ApJ*, 982, 14
- Heintz K. E., et al., 2023, *Nature Astronomy*, 7, 1517
- Heintz K. E., et al., 2024, *Science*, 384, 890
- Heintz K. E., et al., 2025, *A&A*, 693, A60
- Herrera-Camus R., et al., 2025, *A&A*, 699, A80
- Hopkins P. F., Kereš D., Oñorbe J., Faucher-Giguère C.-A., Quataert E., Murray N., Bullock J. S., 2014, *MNRAS*, 445, 581
- Hopkins P. F., et al., 2023, *MNRAS*, 525, 2241
- Hsiao T. Y.-Y., et al., 2023, *ApJ*, 949, L34
- Hsiao T. Y.-Y., et al., 2024a, *ApJ*, 973, 8
- Hsiao T. Y.-Y., et al., 2024b, *ApJ*, 973, 81
- Hsiao T. Y.-Y., et al., 2025, *ApJ*, 993, 70
- Huertas-Company M., et al., 2024, *A&A*, 685, A48
- Hunter D. A., Gallagher III J. S., 1990, *ApJ*, 362, 480
- Hutchison T. A., et al., 2025, *arXiv e-prints*, p. arXiv:2512.02000
- Inoue A. K., Shimizu I., Iwata I., Tanaka M., 2014, *MNRAS*, 442, 1805
- Isobe Y., et al., 2023a, *ApJ*, 951, 102
- Isobe Y., Ouchi M., Nakajima K., Harikane Y., Ono Y., Xu Y., Zhang Y., Umeda H., 2023b, *ApJ*, 956, 139
- Ivey L. R., et al., 2026, *MNRAS*, 546, stag094
- Iyer K. G., et al., 2020, *MNRAS*, 498, 430
- Izotov Y. I., Stasińska G., Meynet G., Guseva N. G., Thuan T. X., 2006, *A&A*, 448, 955
- Jakobsen P., et al., 2022, *A&A*, 661, A80
- Ji X., Belokurov V., Maiolino R., Monty S., Isobe Y., Kravtsov A., McClymont W., Übler H., 2026, *MNRAS*, 545, staf2110
- Johnson B. D., Leja J., Conroy C., Speagle J. S., 2021, *ApJS*, 254, 22
- Jones G. C., et al., 2024a, *arXiv e-prints*, p. arXiv:2412.15027
- Jones G. C., et al., 2024b, *A&A*, 682, A122
- Jones G. C., et al., 2025a, *arXiv e-prints*, p. arXiv:2509.20455
- Jones G. C., et al., 2025b, *arXiv e-prints*, p. arXiv:2512.05213
- Jones G. C., et al., 2025c, *MNRAS*, 540, 3311
- Juodžbalis I., et al., 2025, *arXiv e-prints*, p. arXiv:2504.03551
- Kashikawa N., et al., 2002, *PASJ*, 54, 819
- Kashino D., Lilly S. J., Matthee J., Eilers A.-C., Mackenzie R., Bordoloi R., Simcoe R. A., 2023, *ApJ*, 950, 66
- Kennicutt Jr. R. C., 1998, *ARA&A*, 36, 189
- Kennicutt R. C., Evans N. J., 2012, *ARA&A*, 50, 531
- Kereš D., Katz N., Weinberg D. H., Davé R., 2005, *MNRAS*, 363, 2
- Kewley L. J., Dopita M. A., 2002, *The Astrophysical Journal Supplement Series*, 142, 35
- Kewley L. J., Ellison S. L., 2008, *ApJ*, 681, 1183
- Kimble R. A., MacKenty J. W., O'Connell R. W., Townsend J. A., 2008,

- in Space Telescopes and Instrumentation 2008: Optical, Infrared, and Millimeter. p. 70101E, doi:10.1117/12.789581
- Lamperti I., et al., 2024, *A&A*, 691, A153
- Langeroodi D., Hjorth J., 2023, *arXiv e-prints*, p. arXiv:2307.06336
- Langeroodi D., Hjorth J., 2024, *arXiv e-prints*, p. arXiv:2404.13045
- Langeroodi D., et al., 2023, *ApJ*, 957, 39
- Laseter I. H., et al., 2024, *A&A*, 681, A70
- Le Fèvre O., et al., 2020, *A&A*, 643, A1
- Leja J., Carnall A. C., Johnson B. D., Conroy C., Speagle J. S., 2019, *ApJ*, 876, 3
- Levesque E. M., Richardson M. L. A., 2014, *ApJ*, 780, 100
- Li H., et al., 2018, *MNRAS*, 476, 1765
- Li J., et al., 2025, *ApJ*, 981, 19
- Lilly S. J., Carollo C. M., Pipino A., Renzini A., Peng Y., 2013, *ApJ*, 772, 119
- Looser T. J., et al., 2024, *Nature*, 629, 53
- Looser T. J., et al., 2025, *A&A*, 697, A88
- Luridiana V., Morisset C., Shaw R. A., 2015, *A&A*, 573, A42
- Lützgendorf N., et al., 2022, in Coyle L. E., Matsuura S., Perrin M. D., eds, Society of Photo-Optical Instrumentation Engineers (SPIE) Conference Series Vol. 12180, Space Telescopes and Instrumentation 2022: Optical, Infrared, and Millimeter Wave. p. 121800Y (arXiv:2208.05355), doi:10.1117/12.2630069
- Ma X., et al., 2018, *MNRAS*, 478, 1694
- Maiolino R., Mannucci F., 2019, *A&ARv*, 27, 3
- Maiolino R., et al., 2008, *A&A*, 488, 463
- Marconcini C., et al., 2024, *MNRAS*, 533, 2488
- Marconcini C., et al., 2025, *A&A*, 699, A154
- Marconi A., et al., 2024, *A&A*, 689, A78
- Marshall M. A., et al., 2023, *A&A*, 678, A191
- Marshall M. A., et al., 2025a, *A&A*, 702, A50
- Marshall M. A., et al., 2025b, *A&A*, 702, A174
- Mascia S., et al., 2023, *A&A*, 672, A155
- Mason C. A., Trenti M., Treu T., 2023, *MNRAS*, 521, 497
- Matharu J., et al., 2024, *A&A*, 690, A64
- Mazzolari G., et al., 2024, *A&A*, 691, A345
- Mazzolari G., et al., 2025, *A&A*, 700, A12
- McClymont W., et al., 2024, *MNRAS*, 532, 2016
- McClymont W., et al., 2025a, *MNRAS*, 544, 513
- McClymont W., et al., 2025b, *MNRAS*, 544, 513
- McClymont W., et al., 2026, *MNRAS*, 545, staf2092
- Miller T. B., et al., 2025, *ApJ*, 988, 196
- Morishita T., et al., 2024, *ApJ*, 971, 43
- Mott A., Spitoni E., Matteucci F., 2013, *MNRAS*, 435, 2918
- Mowla L., et al., 2022, *ApJ*, 937, L35
- Mowla L., et al., 2024, *Nature*, 636, 332
- Nagao T., Maiolino R., Marconi A., 2006, *A&A*, 459, 85
- Naidu R. P., et al., 2025, *arXiv e-prints*, p. arXiv:2505.11263
- Nakajima K., et al., 2022, *ApJS*, 262, 3
- Nakajima K., Ouchi M., Isobe Y., Harikane Y., Zhang Y., Ono Y., Umeda H., Oguri M., 2023, *ApJS*, 269, 33
- Nakajima K., et al., 2025, *arXiv e-prints*, p. arXiv:2506.11846
- Napolitano L., et al., 2025, *A&A*, 693, A50
- Noll S., Burgarella D., Giovannoli E., Buat V., Marcellac D., Muñoz-Mateos J. C., 2009, *A&A*, 507, 1793
- Oesch P. A., et al., 2023, *MNRAS*, 525, 2864
- Oke J. B., Gunn J. E., 1983, *ApJ*, 266, 713
- Osterbrock D. E., 1989, *Astrophysics of gaseous nebulae and active galactic nuclei*
- Ozaki S., et al., 2020, *PASJ*, 72, 97
- Papovich C., et al., 2022, *ApJ*, 937, 22
- Parlanti E., et al., 2025a, *arXiv e-prints*, p. arXiv:2512.14844
- Parlanti E., et al., 2025b, *A&A*, 695, A6
- Pascalau R. G., et al., 2025, *arXiv e-prints*, p. arXiv:2505.06349
- Pérez-González P. G., et al., 2025, *Nature Astronomy*, 9, 1240
- Pérez-Montero E., Hägele G. F., Contini T., Díaz Á. I., 2007, *MNRAS*, 381, 125
- Perna M., et al., 2023, *A&A*, 679, A89
- Perna M., et al., 2025, *A&A*, 696, A59
- Péroux C., Howk J. C., 2020, *ARA&A*, 58, 363
- Planck Collaboration et al., 2020, *A&A*, 641, A6
- Pollock C. L., et al., 2025, *arXiv e-prints*, p. arXiv:2506.15779
- Price S. H., et al., 2025, *ApJ*, 982, 51
- Puskás D., et al., 2025a, *arXiv e-prints*, p. arXiv:2510.14743
- Puskás D., et al., 2025b, *MNRAS*, 540, 2146
- Rauscher B. J., et al., 2017, *PASP*, 129, 105003
- Reddy N. A., et al., 2022, *ApJ*, 926, 31
- Reddy N. A., Topping M. W., Sanders R. L., Shapley A. E., Brammer G., 2023, *ApJ*, 952, 167
- Rigby J., et al., 2023, *PASP*, 135, 048001
- Roberts-Borsani G., et al., 2023, *Nature*, 618, 480
- Robertson B. E., et al., 2023, *Nature Astronomy*, 7, 611
- Rodríguez Del Pino B., et al., 2024, *A&A*, 684, A187
- Rodríguez Del Pino B., et al., 2026, *arXiv e-prints*, p. arXiv:2601.06255
- Roper W. J., Lovell C. C., Vijayan A. P., Marshall M. A., Irodotou D., Kuusisto J. K., Thomas P. A., Wilkins S. M., 2022, *MNRAS*, 514, 1921
- Sánchez S. F., et al., 2017, *MNRAS*, 469, 2121
- Sanders R. L., et al., 2016, *ApJ*, 816, 23
- Sanders R. L., et al., 2023a, *ApJ*, 943, 75
- Sanders R. L., Shapley A. E., Topping M. W., Reddy N. A., Brammer G. B., 2023b, *ApJ*, 955, 54
- Sanders R. L., Shapley A. E., Topping M. W., Reddy N. A., Brammer G. B., 2024, *ApJ*, 962, 24
- Sanders R. L., et al., 2025, *arXiv e-prints*, p. arXiv:2508.10099
- Scarlata C., Hayes M., Panagia N., Mehta V., Haardt F., Bagley M., 2024, *arXiv e-prints*, p. arXiv:2404.09015
- Schaerer D., Marques-Chaves R., Xiao M., Korber D., 2024, *A&A*, 687, L11
- Schaye J., et al., 2010, *MNRAS*, 402, 1536
- Scholte D., et al., 2025, *MNRAS*, 540, 1800
- Scholtz J., et al., 2025a, *arXiv e-prints*, p. arXiv:2507.17809
- Scholtz J., et al., 2025b, *MNRAS*, 539, 2463
- Scholtz J., et al., 2025c, *A&A*, 697, A175
- Schwarz G., 1978, *Annals of Statistics*, 6, 461
- Shajib A. J., Treu T., Melo A., Roberts-Borsani G., Knabel S., Cappellari M., Frieman J. A., 2025, *A&A*, 702, L12
- Shapley A. E., et al., 2017, *ApJ*, 846, L30
- Shapley A. E., Sanders R. L., Reddy N. A., Topping M. W., Brammer G. B., 2023, *ApJ*, 954, 157
- Shapley A. E., et al., 2025, *ApJ*, 981, 167
- Shen X., et al., 2024, *MNRAS*, 534, 1433
- Shibuya T., Ouchi M., Harikane Y., 2015, *ApJS*, 219, 15
- Shivaei I., et al., 2020, *ApJ*, 899, 117
- Somerville R. S., Davé R., 2015, *ARA&A*, 53, 51
- Sparre M., Hayward C. C., Feldmann R., Faucher-Giguère C.-A., Muratov A. L., Kereš D., Hopkins P. F., 2017, *MNRAS*, 466, 88
- Stephenson H. M. O., et al., 2025, *MNRAS*, 544, 1412
- Stiavelli M., et al., 2025, *ApJ*, 981, 136
- Straat V., et al., 2023, *ApJ*, 949, L23
- Sun G., Faucher-Giguère C.-A., Hayward C. C., Shen X., Wetzel A., Cochrane R. K., 2023, *ApJ*, 955, L35
- Sun X., et al., 2025, *ApJ*, 986, 179
- Sutherland R. S., Dopita M. A., 2017, *ApJS*, 229, 34
- Sánchez-Blázquez P., et al., 2006, *Monthly Notices of the Royal Astronomical Society*, 371, 703
- Tacchella S., Forbes J. C., Caplar N., 2020, *MNRAS*, 497, 698
- Tacchella S., et al., 2023, *MNRAS*, 522, 6236
- Tang M., et al., 2023, *MNRAS*, 526, 1657
- Topping M. W., et al., 2024, *MNRAS*, 529, 3301
- Topping M. W., et al., 2025a, *MNRAS*, 541, 1707
- Topping M. W., et al., 2025b, *ApJ*, 980, 225
- Torralba A., et al., 2025, *arXiv e-prints*, p. arXiv:2510.00103
- Tremonti C. A., et al., 2004, *ApJ*, 613, 898
- Tripodi R., et al., 2024, *A&A*, 692, A184
- Troncoso P., et al., 2014, *A&A*, 563, A58
- Trump J. R., et al., 2023, *ApJ*, 945, 35
- Übler H., et al., 2023, *A&A*, 677, A145

- Übler H., et al., 2024, *MNRAS*, **533**, 4287
 Übler H., et al., 2025, *arXiv e-prints*, p. arXiv:2509.21575
 Valentino F., et al., 2023, *ApJ*, **947**, 20
 Valentino F., et al., 2025, *A&A*, **699**, A358
 Vallee J. P., 2022, *International Journal of Astronomy and Astrophysics*, **12**, 281
 Vanzella E., et al., 2023, *A&A*, **678**, A173
 Venturi G., et al., 2024, *A&A*, **691**, A19
 Venturi G., et al., 2025, *arXiv e-prints*, p. arXiv:2512.09996
 Wang B., et al., 2023a, *ApJ*, **944**, L58
 Wang B., et al., 2023b, *ApJ*, **957**, L34
 Weinberger R., et al., 2017, *MNRAS*, **465**, 3291
 Witstok J., Smit R., Maiolino R., Curti M., Laporte N., Massey R., Richard J., Swinbank M., 2021, *MNRAS*, **508**, 1686
 Witten C., et al., 2025, *MNRAS*, **537**, 112
 Wolfe A. M., Jorgenson R. A., Robishaw T., Heiles C., Prochaska J. X., 2008, *Nature*, **455**, 638
 Yajima H., Abe M., Fukushima H., Ono Y., Harikane Y., Ouchi M., Hashimoto T., Khochfar S., 2023, *MNRAS*, **525**, 4832
 Yang L., et al., 2025, *ApJS*, **281**, 68
 Zamora S., et al., 2025a, *arXiv e-prints*, p. arXiv:2512.09022
 Zamora S., et al., 2025b, *A&A*, **702**, A102
 Zavala J. A., et al., 2025, *Nature Astronomy*, **9**, 155
 Zhang K., et al., 2017, *MNRAS*, **466**, 3217
 de Graaff A., et al., 2024a, *A&A*, **684**, A87
 de Graaff A., Pillepich A., Rix H.-W., 2024b, *ApJ*, **967**, L40
 van Dokkum P. G., 2001, *PASP*, **113**, 1420
 van der Wel A., et al., 2022, *ApJ*, **936**, 9

¹ *Kavli Institute for Cosmology, University of Cambridge, Madingley Road, Cambridge CB3 0HA, UK*

² *Cavendish Laboratory – Astrophysics Group, University of Cambridge, 19 JJ Thomson Avenue, Cambridge CB3 0HE, UK*

³ *Department of Physics and Astronomy, University College London, Gower Street, London WC1E 6BT, UK*

⁴ *Waseda Research Institute for Science and Engineering, Faculty of Science and Engineering, Waseda University, 3-4-1, Okubo, Shinjuku, Tokyo 169-8555, Japan*

⁵ *Centro de Astrobiología (CAB), CSIC-INTA, Ctra. de Ajalvir km 4, Torrejón de Ardoz, E-28850, Madrid, Spain*

⁶ *Sub-Department of Astrophysics, Department of Physics, University of Oxford, Denys Wilkinson Building, Keble Road, Oxford, OX1 3RH, UK*

⁷ *Sorbonne Université, CNRS, UMR 7095, Institut d’Astrophysique de Paris, 98 bis bd Arago, 75014 Paris, France*

⁸ *Max-Planck-Institut für extraterrestrische Physik (MPE), Gießenbachstraße 1, 85748 Garching, Germany* ⁹ *INAF - Osservatorio Astrofisico di Arcetri, largo E. Fermi 5, 50127 Firenze, Italy*

¹⁰ *European Space Agency, c/o Space Telescope Science Institute, 3700 San Martin Drive, Baltimore MD 21218, USA*

¹¹ *Scuola Normale Superiore, Piazza dei Cavalieri 7, I-56126 Pisa, Italy*

¹² *Association of Universities for Research in Astronomy (AURA) Inc. for the European Space Agency (ESA)*

¹³ *Center for Astrophysical Sciences, Department of Physics and Astronomy, The Johns Hopkins University, 3400 N Charles St. Baltimore, MD 21218, USA*

¹⁴ *European Southern Observatory, Karl Schwarzschild Straße 2, D-85748 Garching bei München, Germany*

¹⁵ *Department of Astronomy, University of Texas, Austin TX 78712, USA*

¹⁶ *Dipartimento di Fisica e Astronomia, Università di Firenze, Via G. Sansone 1, 50019, Sesto F.no (Firenze), Italy*

¹⁷ *Cosmic Dawn Center (DAWN), Copenhagen, Denmark*

¹⁸ *Niels Bohr Institute, University of Copenhagen, Jagtvej 128 DK-2200, Copenhagen, Denmark*

APPENDIX A: EMISSION LINE MAPS

This appendix presents images of integrated fluxes maps for a number of key rest-frame optical emission lines, together with the corresponding wavelength slices of the datacube. All these maps show that high-ionisation and Balmer recombination emission are mostly constrained to the very central part of MACS0647-JD1. The central region between the two stellar clumps (Fig. 2b) hosts the most intense recent star-formation activity, and, consequently, the most intense line emission. In contrast, the outskirts of the system show more pronounced emission from the low-ionisation gas traced via [O II] λ 3726, 3729 emission.

APPENDIX B: FURTHER SPATIALLY RESOLVED EMISSION LINES DIAGNOSTICS

In Fig. B1, we report spaxel-by-spaxel maps of O33 and O32 diagnostic ratios (as defined in the main text of Sec. 4.2 and following the criteria and demarcation lines identified by Mazzolari et al. 2024). In the case of both diagnostics, all spaxels reside below the ‘AGN only’ regime, revealing that AGN is likely not the main excitation source of the ISM in neither region of this galaxy.

APPENDIX C: ON THE VELOCITY FIELD OF MACS0647-JD1

In Fig. C2a, we present the spatially resolved maps of Δv (velocity shift of a particular spaxel with respect to galaxy’s systemic velocity). We obtain Δv from the MCMC fitted redshift corresponding to each spaxel spectrum:

$$(1 + z_{\text{pix}}) = (1 + z_{\text{pix,med}}) \times (1 + \Delta v/c) . \quad (\text{C1})$$

Here, the median redshift of the spaxels is $z_{\text{pix,med}} = 10.1672$. The fact that the direction of the rotational gradient approximately coincides with the direction of IFU slicers, together with the relatively small amplitude of 160 km s^{-1} (~ 1.45 spectral pixels, peak-to-peak) makes it uncertain whether the observed rotation is a real feature. This issue has been identified and documented (symptom NS-IFU07⁶) but no official solution has been proposed to date. Similar artificial rotation patterns have been reported in ground-based IFU observations obtained with the Subaru/FOCAS instrument (Kashikawa et al. 2002; Ozaki et al. 2020) and, more recently, in high spectral resolution IFU studies of high-redshift galaxies. In particular, Isobe et al. (2023a) demonstrated that a differential effective slit width across the IFU slices can introduce spurious velocity gradients aligned with the instrumental geometry, thereby mimicking ordered rotation in emission-line velocity fields.

While the geometrical model implemented within the current pipeline typically succeeds in providing an accurate wavelength calibration (Dorner et al. 2016; Lützgendorf et al. 2022), a recent report by Beck (2025) argues that some imperfections in the current IFU

⁶ <https://jwst-docs.stsci.edu/known-issues-with-jwst-data/nirspec-known-issues/nirspec-ifu-known-issues/>

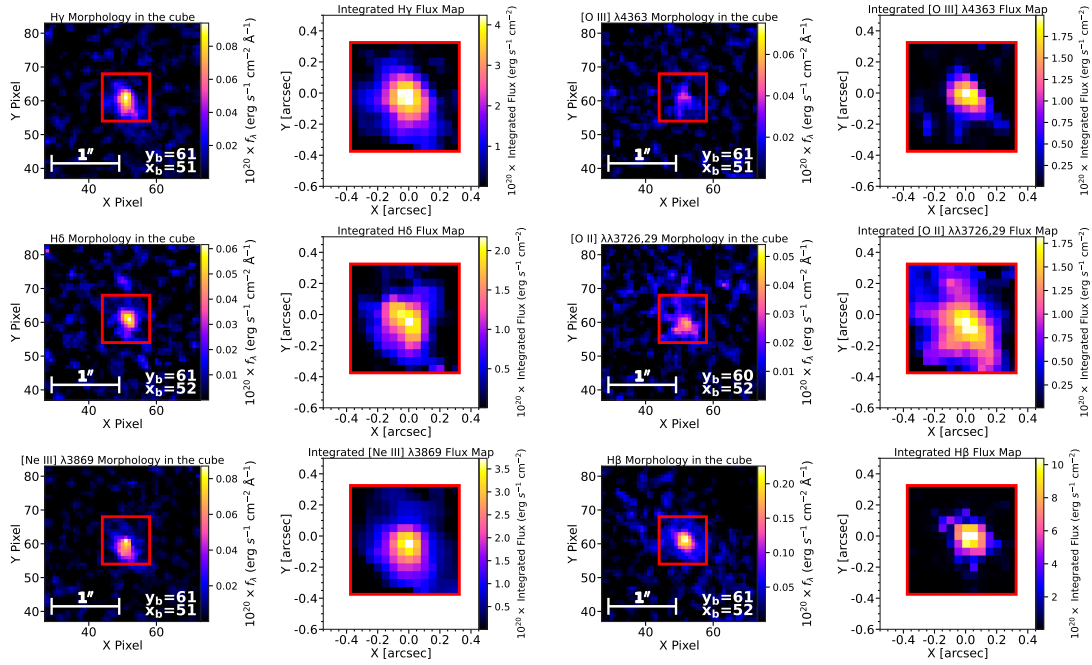


Figure A1. This figure displays a comparison between the images obtained by collapsing the PSF-matched datacube (see Sec. 3.1 for details of the PSF matching method) along the wavelength slices corresponding to our key emission lines and the images resulting from mapping out the integrated fluxes of these emission lines which were determined by our MCMC spectral fitting analysis. We remark on small shifts between the centroids of different emission lines (identified by the coordinates y_b and x_b of the brightest spaxel for each emission line map) but this is not worrying given that these differences are on the order of ~ 1 spaxel. This centroid drift as a function of wavelength is likely to be caused by a combination of filter transmission effects and imperfect NIRSpec/IFU calibrations.

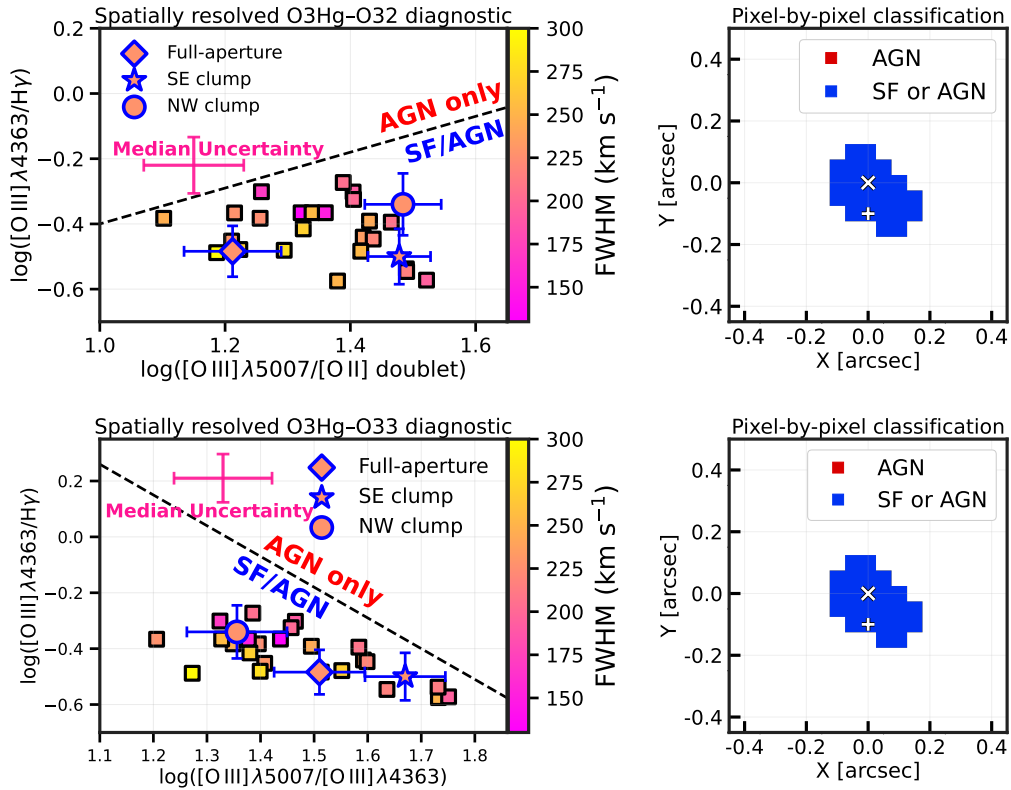


Figure B1. This diagram is equivalent (in terms of labelling and the meaning of various symbols) to Fig. 6, which presents the O3Hg vs Ne3O2 diagnostic diagram on a spatially resolved spaxel-by-spaxel scale. However, alternative AGN vs SFG diagnostics (Mazzolari et al. 2024) are illustrated: O3Hg-O32 (top panels) and O3Hg-O33 (bottom panels). We can remark that, in contrast to the results based on the diagnostic O3Hg – Ne3O2 (from Fig. 6, showing the presence of a south-southwest AGN-dominated region), if we use either O3Hg – O32 or O3Hg – O33 diagnostics, we would observe that all regions of the MACS0647-JD1 system are either dominated by star-formation driven photoionisation or the contribution of SF and AGN are similar.

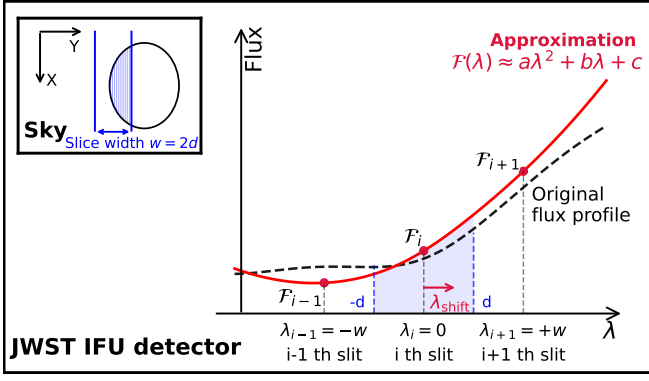


Figure C1. In this figure, we present a simplified explanation of the slit width effect. The main panel shows the flux profile projected onto the JWST NIRSpec/IFU detector (black dashed curve) and the measured fluxes \mathcal{F}_{i-1} , \mathcal{F}_i and \mathcal{F}_{i+1} on three adjacent slices. In this approach, the original flux profile is approximated with a quadratic function (the red solid curve) within a wavelength range $-w < \lambda < w$. The inset panel schematically shows an hypothetic circular object on the sky. The X (Y) direction denotes the direction of the slice length (width). The blue lines show the position of the edges of the central slice. The light coming into the slice (blue hatched) is projected onto the detector, and the Y direction in the sky is parallel to the dispersion (or wavelength) direction on the detector.

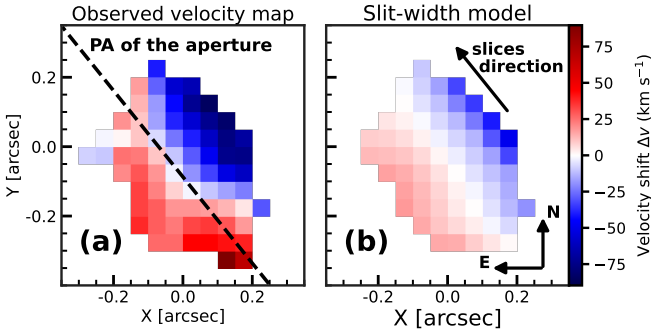


Figure C2. This figure shows the spatially resolved Δv (the velocity field) map derived from single-Gaussian component spaxel-by-spaxel spectral fits (Fig. C2a). We only show the spaxels with a solid detection of H γ ($S/N > 5$). We also indicate the position angle of the aperture of these observations, $PA = 38.83^\circ$, i.e. the direction of the NIRSpec/IFU slices. The velocity gradient of the observed rotational pattern is perpendicular to the direction of the slices. In Fig. C2b, we show a mock velocity pattern resulting from the IFU slices geometrical model described in the text.

spectral distortion model remain. Artificial kinematics shifts are observed for multiple grating/filter combinations and regardless of the cube weighting algorithms (‘drizzle’, ‘EMSM’ or ‘MSM’). In the particular case of G395M grating that we used in our observations, Beck (2025) reports a peak-to-peak amplitude of the artificial kinematic shift of ~ 1.6 spectral pixels in the case of a planetary nebula with substantially lower intrinsic kinematics. This is similar to the amplitude of the velocity gradient in Fig. C2a. However, it should be noted that the rotational pattern observed in our case is both more spatially extended (and larger than the PSF size), but also significantly less noisy (as there are less large kinematic variations in adjacent spaxels) than the pattern reported by Beck (2025).

In Fig. C2b, we show that a simple geometrical model of the IFU slicer configuration (that is described and explained schematically in Fig. C1) can reproduce an artificial velocity pattern similar in amplitude and orientation to that observed in our data. The underlying

effect arises from spatial variations in the emission-line surface brightness across the finite width of an IFU slice (Bacon et al. 1995). If we have a slice of projected width w on the IFU detector and with a flux profile $\mathcal{F}(\lambda)$ along the dispersion (wavelength) direction coordinate λ (perpendicular to the slit width direction), the effective centroid of the detected emission line can be shifted relative to the true wavelength. The method to quantify the magnitude of this wavelength shift is thoroughly described in Isobe et al. (2023a), but here we give an outline of the numerical calculations. We can estimate the wavelength shift caused by the slit-width effect from a barycenter of the flux following a $\mathcal{F}(\lambda)$ profile intercepted by the slice:

$$\lambda_{\text{shift}} = \frac{\int_{-w/2}^{+w/2} \lambda \times \mathcal{F}(\lambda) d\lambda}{\int_{-w/2}^{+w/2} \mathcal{F}(\lambda) d\lambda} \quad (\text{C2})$$

where λ denotes the dispersion-axis coordinate across the projected slice width rather than the wavelength. This expression captures the fact that asymmetric illumination of the slice can bias the measured wavelength centroid. Following Isobe et al. (2023a), and assuming that $\mathcal{F}(\lambda)$ can be locally approximated by a second-order polynomial ($\mathcal{F}(\lambda) \approx a\lambda^2 + b\lambda + c$), then Equation (C2) can be simplified by performing the integration:

$$\lambda_{\text{shift}} = w \times \frac{bw}{aw^2 + 12c} \quad (\text{C3})$$

We then consider three adjacent IFU slices on the detector, at the dispersion axis coordinates $\lambda_{i-1} = -w$, $\lambda_i = 0$ and $\lambda_{i+1} = +w$, such that the central wavelength slice ‘i’ contains the peak of H γ emission. The fluxes measured in each of these slices are therefore:

$$\mathcal{F}_{i+1} \equiv \mathcal{F}(\lambda_{i+1}) = aw^2 + bw + c \quad (\text{C4})$$

$$\mathcal{F}_{i-1} \equiv \mathcal{F}(\lambda_{i-1}) = aw^2 - bw + c \quad (\text{C5})$$

$$\mathcal{F}_i \equiv \mathcal{F}(\lambda_i) = c \quad (\text{C6})$$

Using these three parametrisation equations for the fluxes observed on the three adjacent slices, we can further simplify Equation (C3):

$$\lambda_{\text{shift}} = w \times \frac{\mathcal{F}_{i+1} - \mathcal{F}_{i-1}}{\mathcal{F}_{i+1} + 22 \times \mathcal{F}_i + \mathcal{F}_{i-1}}, \quad (\text{C7})$$

This formulation provides an estimate of the wavelength bias induced by slice-to-slice flux gradients. For JWST/NIRSpec, the undispersed IFU slices are 2 pixels wide according to JWST documentation⁷. Using the spectral dispersion and line-spread function appropriate for the observed H γ wavelength, this corresponds to an effective projected width of $w \approx 35.8 \text{ \AA}$. The peak-to-peak amplitude of the rotational pattern resulting from our slit geometry model is $\approx 55 \text{ km s}^{-1}$, ~ 3.2 times smaller than in the observed data ($\approx 175 \text{ km s}^{-1}$). However, if we compare the 5th – 95th percentiles amplitudes, the discrepancy is reduced (114 km s^{-1} in the observed data and 44 km s^{-1} in our simple model). We emphasize that our implementation represents

⁷ <https://jwst-docs.stsci.edu/jwst-near-infrared-spectrograph/nirspec-observing-modes/nirspec-ifu-spectroscopy>

a highly simplified, first-order description of the IFU slit geometry and does not capture more subtle instrumental effects or deviations of the slit geometry from a simple, parametric form. Consequently, while instrumental systematics may plausibly account for a substantial fraction of the observed velocity gradient, we are not able to fully rule out the hypothesis that this kinematic pattern might be real, which could imply that the MACS0647-JD1 system would consist of two bright clumps within the same rotating disc.

APPENDIX D: PROSPECTOR SED FITS OF SPECTROSCOPY AND PHOTOMETRY

In [Fig. D1](#) and [Fig. D2](#), we show our results from the PROSPECTOR fits based on the spectra and photometric fluxes corresponding to the apertures of the two stellar components (SE-C and NW-C in [Fig. 2b](#)). Our fitting method is described in [Section 3.3](#).

This paper has been typeset from a $\text{\TeX}/\text{\LaTeX}$ file prepared by the author.

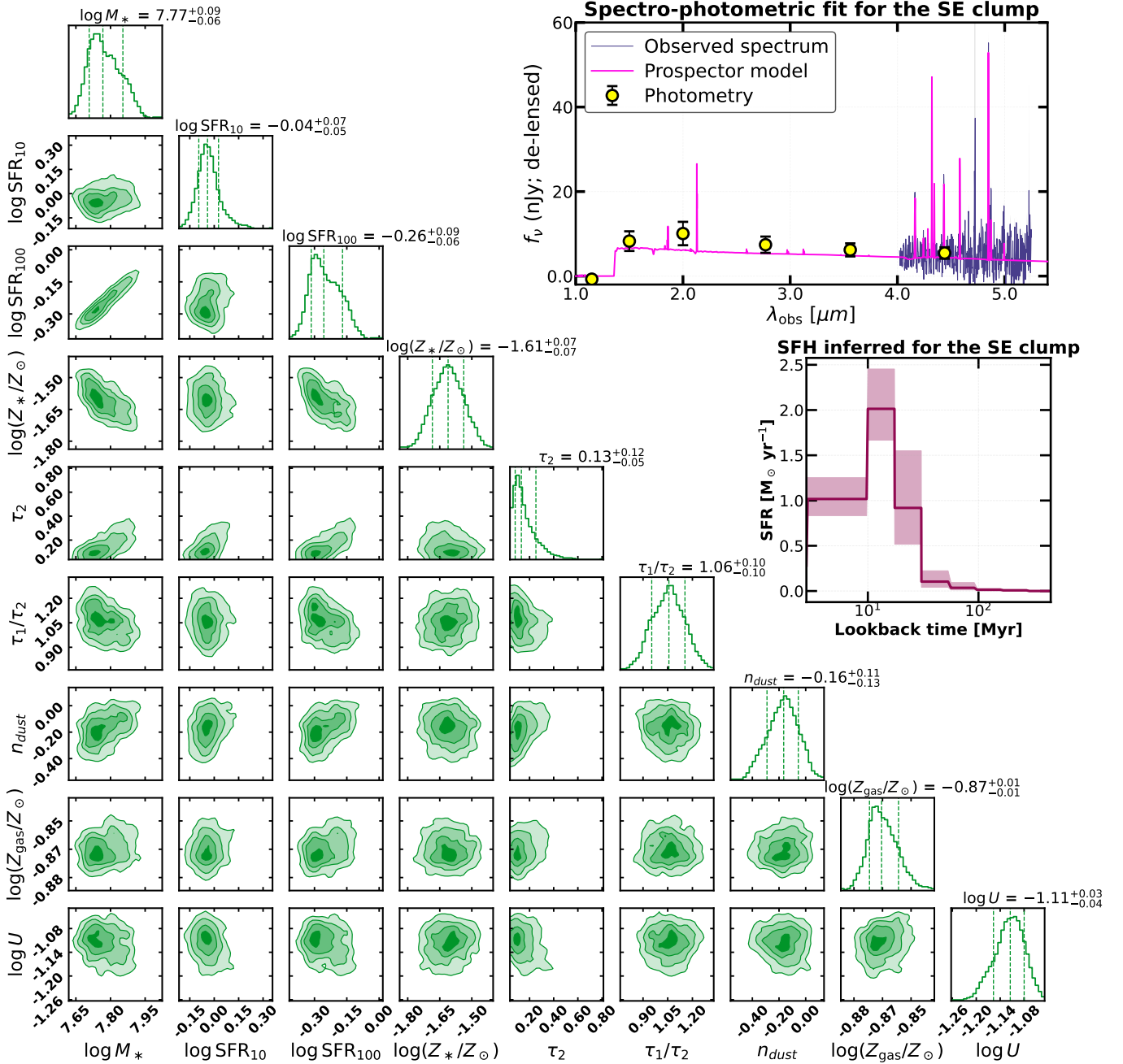


Figure D1. In this figure, we present the PROSPECTOR fitting results for the more massive stellar component (the south-east clump). The corner plot displays the marginalised one-dimensional posterior distribution and the two-dimensional correlations involving the following parameters: the logarithm of the stellar mass (in solar masses), the logarithms of SFR averaged over the 10 Myr or 100 Myr prior to observation (in $M_\odot \text{ yr}^{-1}$), stellar metallicity, the optical depth of the diffuse ISM (τ_2), the extra-additional factor of attenuation towards the birth clouds (τ_1/τ_2), the dust attenuation curve slope, n_{dust} , the gas-phase metallicity and the ionisation parameter. The top-right inset panel shows the resulting SED model for the SE clump, while the central-right inset panel displays the SFH inferred by PROSPECTOR.

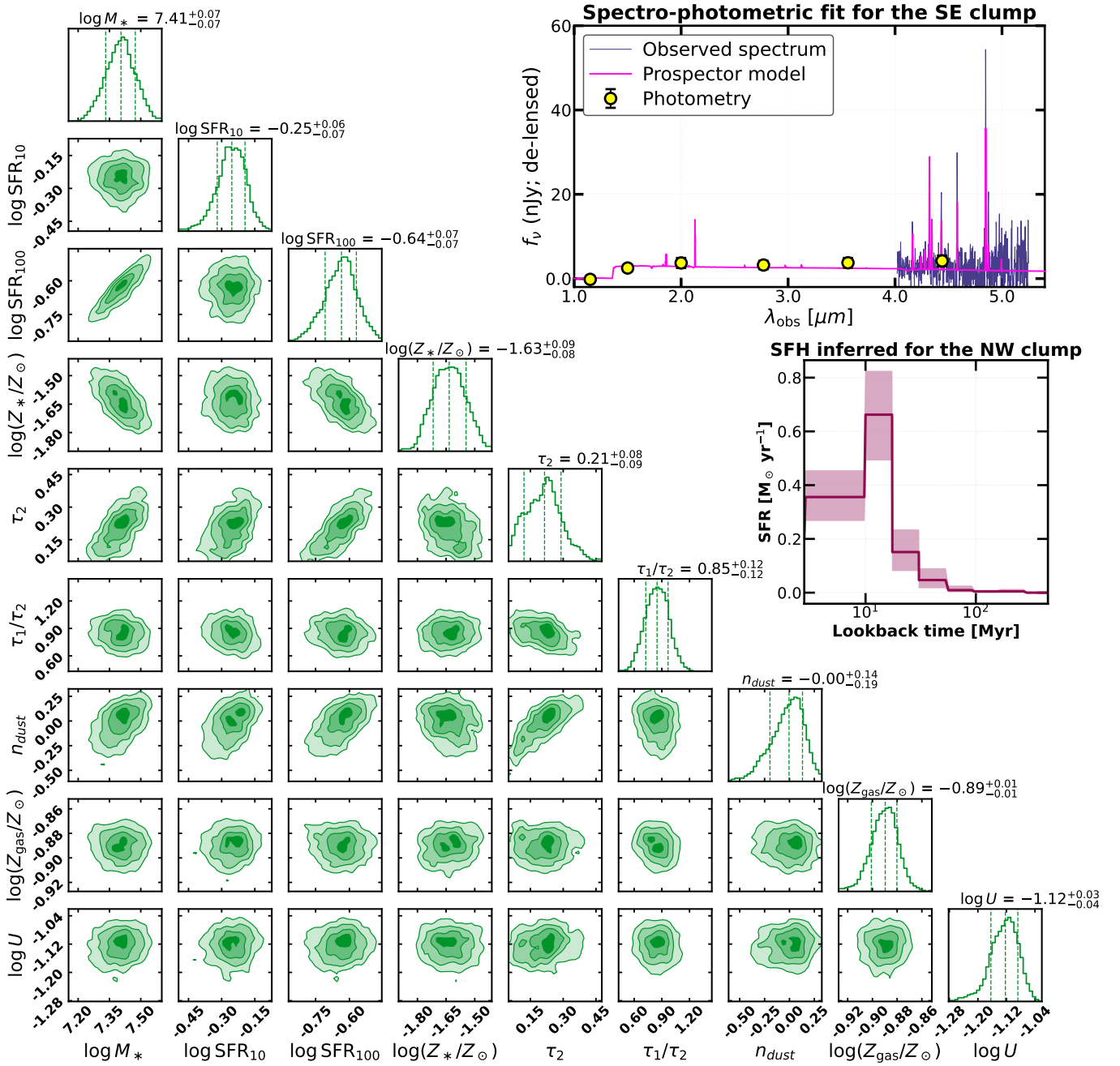


Figure D2. This figure is equivalent to [Fig. D1](#), but it shows the PROSPECTOR best-fit parameters in the case of the less massive stellar component (the north-west clump). The top-right inset panel shows the SED model for the NW clump, while the central-right inset panel displays the SFH inferred by PROSPECTOR.